

AN ABSTRACT OF THE THESIS OF

Ashley Diane Mason for the degree of Master of Science in
Electrical and Computer Engineering presented on June 13, 2011.

Title: Effects of Ultraviolet Illumination and a Parylene-A Activation Layer
on the Gas Phase Sensing Characteristics of ZnO Nanobridges

Abstract approved: _____

John F. Conley, Jr.

ZnO nanowires (NWs) are good candidates for chemical sensing because of their high surface-to-volume ratio. In this work, ZnO nanobridge sensors were fabricated utilizing a novel method which uses carbonized photoresist (C-PR) as a nucleation layer. The use of C-PR allows simultaneous growth and integration of NWs to lithographically-defined features. The nanobridge sensors are shown to be sensitive to the presence of O₂, H₂O, CO, and H₂/N₂ gas. However, since ZnO dissolves in water, a protective layer is necessary for these sensors to be used in the liquid or vapor phase. A chemical vapor deposition (CVD) process for amino-[2,2]paracyclophane (parylene-A) was developed and used to successfully protect the NWs. Gas sensing measurements were performed on bare and parylene-A coated devices with and without UV illumination. The parylene-A layer was found to attenuate sensitivity to O₂ and H₂O, and UV illumination was found to decrease the response time.

©Copyright by Ashley Diane Mason
June 13, 2011
All Rights Reserved

Effects of Ultraviolet Illumination and a Parylene-A
Activation Layer on the Gas Phase Sensing Characteristics of
ZnO Nanobridges

by

Ashley Diane Mason

A THESIS

submitted to

Oregon State University

in partial fulfillment of
the requirements for the
degree of

Master of Science

Presented June 13, 2011
Commencement June 2012

Master of Science thesis of Ashley Diane Mason presented on June 13, 2011.

APPROVED:

Major Professor, representing Electrical and Computer Engineering

Director of the School of Electrical Engineering and Computer Science

Dean of the Graduate School

I understand that my thesis will become part of the permanent collection of Oregon State University libraries. My signature below authorizes release of my thesis to any reader upon request.

Ashley Diane Mason, Author

ACKNOWLEDGEMENTS

I would like to thank my major advisor and graduate committee for their guidance and advice throughout the course of my Master of Science. In addition, I would like to thank all of the post-doctoral, graduate, and undergraduate students I have had the privilege to work with. Throughout the course of this work, a number of colleagues and friends have been there to pick my brain, help me fix whatever was broken, challenge me, and support me. Thank you all! Last and definitely not least, I would like to thank my parents; I wouldn't be here without them!

Funding for this work was provided by the U.S. Army Research Laboratory (W911NF-07-2-0083), the Office of Naval Research (N00014-07-1-0457), the Oregon Nanoscience and Microtechnologies Institute (ONAMI), the National Science Foundation (through an REU supplement to NSF DMR 0805372), and an Intel scholarship. Collaborations with Hewlett-Packard, ON Semiconductor, and CEM Corporation also made this work possible.

TABLE OF CONTENTS

	<u>Page</u>
1 Introduction	1
2 Literature Review	3
2.1 Nanowire Growth Methods	3
2.2 Integration Approaches	5
2.3 Sensing Demonstrations	7
2.3.1 Bare Nanowires	7
2.3.2 Coated or Functionalized Nanowires	9
3 Methods and Materials	13
3.1 Base Nanobridge Device Fabrication	13
3.2 Protection of ZnO Nanowires	15
3.3 Electrical Characterization and Gas Sensing	16
4 Results and Discussion	20
4.1 Growth Optimization	20
4.1.1 Effect of Growth Temperature	20
4.1.2 O ₂ Injection	22
4.1.3 Vibratory Milling	22
4.2 Base Device	25
4.2.1 Device Design and Refinements	25
4.3 Parylene-A Coating	35
4.3.1 Physical Characterization	35
4.3.2 Electrical Characterization and Gas Sensing	38
4.3.3 Effect of Continuous UV Illumination on Sensor Response . .	44
5 Summary, Conclusions and Future Work	49
Appendices	54
A Microwave Growth of ZnO Nanowires	55
A.1 Abstract	55
A.2 Introduction	55

TABLE OF CONTENTS (Continued)

	<u>Page</u>
A.3 Experimental Details	57
A.4 Results and Discussion	61
A.4.1 Nanowire Dimensions (Length, Diameter, and Aspect Ratio)	61
A.4.1.1 Length vs Time	61
A.4.1.2 Length vs Concentration	64
A.4.1.3 Longest Wires	66
A.4.1.4 Diameter	67
A.4.1.5 Aspect Ratio	67
A.4.2 Density	68
A.4.3 Orientation	69
A.4.4 Impact of Seed Layer and Substrate	69
A.4.5 Crystallites	73
A.4.6 Process Control	74
A.5 Summary and Conclusions	76

LIST OF FIGURES

Figure		Page
2.1	Selective growth of ZnO on C-PR demonstrated by Cheng <i>et al.</i> [16].	4
2.2	Device fabrication using (a) physical transfer or (b) pick and place methods.	6
3.1	Processing steps for ZnO nanobridge devices.	13
3.2	ZnO nanowire growth set-up.	14
3.3	Common types of parylene.	15
3.4	CVD process used for parylene-A coating.	15
3.5	The NorECs ProboStat used for gas sensing measurements.	17
3.6	Schematic diagram of the gas sensing measurement set-up.	17
3.7	A sample loaded in the NorECs ProboStat showing electrical connections and the inside of the probostat.	18
3.8	The resulting characteristics of the InGaN used for in-situ UV during gas measurements obtained using optical spectroscopy.	19
4.1	SEM images of ZnO NBs grown for 40 minutes using an O ₂ flow rate of 3 sccm, 150 sccm of N ₂ carrier gas, pressure of 1.4 Torr, and a precursor temperature of (a) 925 °C and (b) 930 °C.	21
4.2	SEM images of ZnO NBs grown for 40 minutes using 150 sccm of N ₂ carrier gas, a pressure of 1.4 Torr, precursor temperature of 920 °C and an O ₂ injection flow rate of (a) 5 sccm, (b) 3 sccm, and (c) 1 sccm.	23
4.3	SEM images of ZnO NBs grown for 40 minutes using a precursor temperature of 930 °C, 5 sccm O ₂ , 150 sccm of N ₂ carrier gas, and a pressure of 10 Torr utilizing (a) mortar and pestel mixing, or (b) vibratory milling to mix the precursor.	24
4.4	Top-down schematic of (a) original and (b) revised ZnO NB devices showing C-PR and Mo regions.	26
4.5	Device schematic cross-section showing the NB drain (D), gate (G), and source (S).	26

LIST OF FIGURES (Continued)

<u>Figure</u>		<u>Page</u>
4.6	Plot of UV response for “old” and “new” design 5 μm gap devices where $V_{DS} = 3\text{ V}$, and the gate was left floating. The old device structure is shown in Fig. 4.8(a) and the new device structure is shown in Fig. 4.8(b).	27
4.7	Device revision: Series resistance design (SRD).	28
4.8	Plot of (a) I_D vs V_{DS} in the dark and under UV1 illumination and (b) I_D over time when exposed to 30 seconds of UV1 with $V_{DS} = 3\text{ V}$ for two 5 μm gap SRD NB devices.	29
4.9	Plot of I_D over time for an as prepared and a N_2 cleaned 5 μm gap SRD NB device exposed to 30 seconds of UV1 with $V_{DS} = 3\text{ V}$. . .	31
4.10	Plot of O_2 and H_2O sensing for 5 μm gap SRD NB devices with precursor temperatures of 925 $^\circ\text{C}$ and 930 $^\circ\text{C}$ used during growth. .	32
4.11	Plot of I_D over time when exposed to 30 seconds of UV1 with $V_{DS} = 3\text{ V}$ for a 5 μm gap SRD NB device on glass substrate. . . .	33
4.12	Fluorescence microscopy images of ZnO NWs modified with biotin and FITC conjugated streptavidin.	36
4.13	Dark field microscope images as a function of time for a ZnO NB device coated with biotin left continuously in DI water.	36
4.14	Contact angle measurements on ZnO NWs (a) before and (b) after parylene-A coating.	37
4.15	Darkfield microscope images as a function of time for a ZnO NB device submerged in DI water (a) before and (b) after parylene-A coating.	37
4.16	Plot of (a) I_D vs V_{DS} in the dark and under UV illumination and (b) I_D vs time when periodically exposed to 30 seconds of UV with $V_{DS} = 3\text{ V}$ for a 5 μm gap SRD NB device on a Si/SiO ₂ substrate. .	39
4.17	Plot of O_2 and H_2O response for different flow rates for a 5 μm gap SRD NB device on Si/SiO ₂ where $V_{DS} = 3\text{ V}$	41
4.18	Plot of I_D over time when exposed to 30 seconds of UV with $V_{DS} = 3\text{ V}$ for a 5 μm gap SRD NB device fabricated on a glass substrate. . . .	42

LIST OF FIGURES (Continued)

<u>Figure</u>	<u>Page</u>
4.19 Plot of O ₂ (circles) and H ₂ O (squares) sensing using a 5 μ m gap SRD NB device with $V_{DS} = 3$ V before (open) and after (closed) parylene-A coating.	43
4.20 Plot of (a) O ₂ and (b) H ₂ O sensing using a 5 μ m gap SRD NB device with $V_{DS} = 3$ V before and after parylene-A coating with and without in-situ UV2 illumination.	45
4.21 Plot of the response to a continuous O ₂ flow using a 5 μ m gap SRD NB device with $V_{DS} = 3$ V after parylene-A coating with and without in-situ UV2 illumination.	46
4.22 Plot of the response and recovery for a 5 μ m gap SRD NB device with $V_{DS} = 3$ V after parylene-A coating when O ₂ was turned on/off O ₂ every 300 seconds.	47
4.23 Plot of CO and H ₂ /N ₂ sensing using a 5 μ m gap SRD NB device with $V_{DS} = 3$ V after parylene-A coating with and without in-situ UV2 illumination.	48
5.1 Formation of imines from the amines on an aminosilanized surface [79].	51
5.2 ZnO NB (a) before and (b) after sputtering SiO ₂ on top of the ZnO NWs.	52

LIST OF TABLES

<u>Table</u>		<u>Page</u>
2.1	Metal-oxide nanowire sensors	10
2.2	Metal-enhanced nanowire sensors	11
4.1	UV response of ZnO NWs	34

LIST OF APPENDIX FIGURES

<u>Figure</u>	<u>Page</u>
A.1 Plot of average NW length vs growth time for ZnO NWs grown using various combinations of temperature and precursor concentration on either (a) 90 nm ALD ZnO films on Si or (b) 90 nm ALD ZnO films with a 10 nm thick Al ₂ O ₃ buffer layer (ZnO/Al ₂ O ₃ /Si). Lines are to guide the eye.	62
A.2 SEM images illustrating NW growth on ZnO/Al ₂ O ₃ /Si substrates using a 25 mM (1:1) solution at 85 °C after (a) 1 min, (b) 5 min, (c) 20 min, and (d) 60 min of growth time.	63
A.3 Plot of NW length vs 1:1 precursor concentration for NWs that were grown for either (a) 60 minutes on 90 nm ALD ZnO films on Si or (b) 20 minutes on 90 nm ALD ZnO films with a 10 nm thick Al ₂ O ₃ buffer layer (ZnO/Al ₂ O ₃ /Si). Lines are to guide the eye.	64
A.4 Plot of NW length vs concentration ratio for various precursor concentrations on 90 nm ZnO on Si.	65
A.5 Aspect ratio as a function of growth time for NWs grown on ALD ZnO films with a 10 nm thick Al ₂ O ₃ buffer layer (ZnO/Al ₂ O ₃ /Si) at various temperatures and concentrations. Lines are to guide the eye.	68
A.6 SEM images of Group I (see Table A.1) growth on (a) 15 nm thick ALD ZnO films, (b) 200 nm thick ALD ZnO films, (c) 90 nm ALD ZnO films annealed in N ₂ at 900 °C, (d) 90 nm ALD ZnO films annealed in N ₂ at 400 °C, (e) 90 nm ALD ZnO films annealed in air at 900 °C, and (f) 90 nm sputtered ZnO films.	71
A.7 XRD data showing crystalline peaks for (a) 90 nm ALD ZnO as deposited, (b) 10 nm ALD Al ₂ O ₃ buffer and 90 nm ZnO seed layer as deposited, (c) 90 nm ALD ZnO annealed in N ₂ at 900 °C and (d) 90 nm ALD ZnO annealed in O ₂ at 900 °C. Data is vertically offset for visualization.	73
A.8 Hot plate growths had additional crystallites which covered the surface of the sample as shown in (a). Well-controlled microwave growths were free of unwanted crystallites as shown in (b).	74

LIST OF APPENDIX FIGURES (Continued)

<u>Figure</u>		<u>Page</u>
A.9	Process control effects on growth morphology depicting: (a) well-controlled growth with consistent NW lengths and uniformity across the sample, (b) poorly controlled growth with altered morphology and wide variation in length and (c) a moderately well-controlled growth.	76

LIST OF APPENDIX TABLES

<u>Table</u>	<u>Page</u>
A.1 Seed layer summary	58
A.2 Solution concentrations summary	60

Chapter 1 – Introduction

Nanowires (NWs) are favored for gas sensing because of their increased surface-to-volume ratio (compared to thin-film-based alternatives), which amplifies the role of surface states critical for gas sensing [1]. Metal-oxide NWs have been used to detect a number of gases [2–14] and can be fabricated relatively easily [15]. Although NW-based devices are a highly sensitive platform, the challenges of (i) developing integrated sensors on a full wafer-scale and (ii) creating selective sensors still remain.

Integration of NWs into an electronic device can be achieved by the directed growth of NW nanobridges (NBs). Using this method, NWs are grown from one electrode and terminate on an opposing electrode so electrical contact is achieved simultaneously with growth. In this work, carbonized photoresist (C-PR) is used as a nucleation layer. Cheng *et al.*, demonstrated that ZnO NWs could be selectively grown on C-PR. Using C-PR as a nucleation layer greatly simplifies processing steps and only requires traditional lithography and a high temperature carbonization step prior to NW growth [16]. Huang and Pelatt showed that C-PR could be used to grow ZnO nanobridge devices which could be used for gas and UV sensing [17,18].

Selective sensing requires that a response is only observed in the presence of a target analyte. As a proof of concept for specific sensing, the selective binding

of biotin and streptavidin is commonly exploited [19–22]. In previous work, we demonstrated that biotin could be attached to the ZnO NW surface [23]. However, ZnO dissolves in deionized (DI) water [24] and we found that biotin-coated ZnO dissolved as well [23]. Thus, the focus of this thesis is to investigate potential ways to protect the ZnO NWs.

A commonly used moisture barrier is [2,2] paracyclophane (parylene). In this work, a chemical vapor deposition (CVD) coating process for amino-[2,2] paracyclophane [25, 26] or parylene-A was developed. The amine group on parylene-A is a useful functional group for anchoring aptamers, a small oligonucleotide which can potentially be used to selectively sense a target species [27]. The effect of the parylene-A activation layer on the ZnO NB response to O_2 , H_2O , CO and N_2/H_2 was investigated. It was found that the parylene-A layer attenuates gas sensitivity. The impact of UV illumination on gas sensing was also investigated. UV illumination during sensing was found to enhance device sensitivity. For example, under UV excitation the response time of the device is decreased when exposed to O_2 .

A literature review of nanowire growth methods, device integration approaches, and sensing demonstrations is covered in Chapter 2. The methods and materials for our experiments are presented in Chapter 3. Subsequently, the experimental results including: electrical characterization, results from functionalization with the parylene-A and its impact on sensor performance, and UV-enhancement during gas sensing are discussed in Chapter 4. Lastly, a conclusion section will summarize this thesis and suggestions for future work will be provided.

Chapter 2 – Literature Review

A literature review is included to provide insight into topics relevant to this work. In this section, previous methods of nanowire growth, device fabrication, and previously demonstrated sensor implementations related to this project are presented.

2.1 Nanowire Growth Methods

Currently the predominant methods for nanowire growth are the (i) vapor liquid solid (VLS), (ii) vapor solid (VS), and (iii) solution-based methods. Although there are some variations (laser-assisted growth, molecular beam epitaxy (MBE)), all growth techniques can be broadly categorized into one of these three methods.

In the VLS method, a metal catalyst is used to seed the growth of nanowires. Usually a thin metal film is deposited on a base substrate and heated to a high temperature whereat a catalyst ball forms (the temperature required depends on the metal and substrate used). The growth species has to be evaporated at high temperature (on the order of 1000 °C) to form an alloy with the catalyst ball (liquid) and once the droplet is supersaturated, nanowire nucleation occurs and growth begins [10, 28–31]. Although the VLS method presents a high level of morphology control (through the size of the catalyst droplet), the metal droplet remains on the top of a completely grown nanowire even after growth is complete,

a significant drawback from the standpoint of possible contamination.

The VS method is similar to the VLS growth process in that a high temperature is still needed for evaporation of the growth species, but rather than using a metal catalyst, a seed or nucleation layer is used. Work by Conley *et al.* showed that a patterned ZnO thin film could be used to selectively seed the growth of ZnO NWs [32]. For ZnO NWs, Yao *et al.* explain that in their work the nucleation is likely facilitated by Zn or Zn suboxides [33], and their nanostructures were likely seeded by condensed Zn droplets. Using the VS method it is possible to avoid the issues surrounding metal contamination [32–35]. Another alternative seed layer which successfully circumvents the need for a metal catalyst was demonstrated very recently by Cheng *et al.* and is shown in Fig. 2.1. Carbonized photoresist (C-PR) has been demonstrated as a nucleation layer for selective and oriented growth of ZnO NWs from evaporated ZnO powder [16].

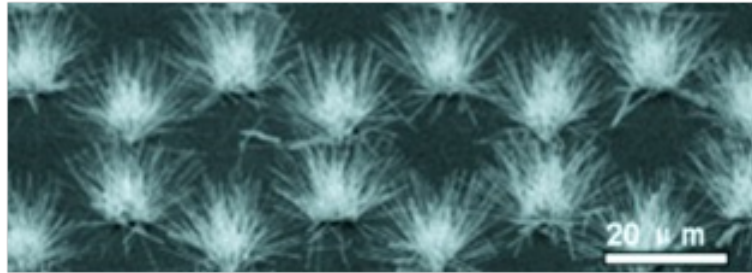


Figure 2.1: Selective growth of ZnO on C-PR demonstrated by Cheng *et al.* [16].

Solution based growth methods are also available for some types of nanowires. $\text{Zn}(\text{NO}_3)_2$ and hexamethylene tetramine (HMT) have been used extensively for hydrothermal growth of ZnO NWs following the work by Vayssieres *et al.* [36]. Although this method facilitates lower temperature growth (approximately 70-

100 °C) and thus opens up possibilities with non-traditional substrates (i.e. flexible substrates), growth times of 20 hours or longer may be necessary using traditional hot-plate heating [37–41]. Recent work by Unalan *et al.* [39] showed that the growth rate can be accelerated using microwave heating. Our work using a microwave featuring direct temperature control for solution phase ZnO nanowire growth is presented in Appendix A.

2.2 Integration Approaches

In order for NWs to be used practically, they must be electrically-connected and integrated into a device structure. The earliest NW-based devices were created using either physical transfer or pick and place methods. In both approaches, NWs were grown on one substrate and transferred to a second device substrate, which may be patterned with electrodes. For physical or mechanical transfer, the device substrate is pushed across the top of a growth sample and friction transfers NWs from one substrate to the other (see Fig. 2.2 (a)). In the pick and place method, NWs are sonicated off of a growth substrate, dispersed in solution, and deposited onto a device substrate (see Fig. 2.2 (b)). Although both physical transfer and pick and place have been used to produce working devices, NW placement is random and device yield is low. Dielectrophoresis (DEP) has been used recently to improve device yield by using a.c. electric fields to align and connect NWs between opposing metal electrodes [42–44]. DEP still requires that NWs be grown on one substrate and integrated into devices on a second substrate.

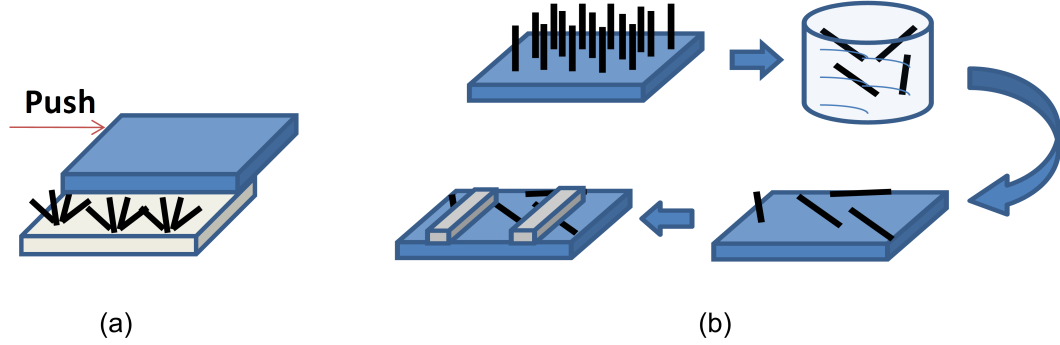


Figure 2.2: Device fabrication using (a) physical transfer or (b) pick and place methods.

Another way to address the issues of random NW placement and low device yield is by creating nanobridges. In this case, NWs are seeded on one electrode and terminate on a second electrode, meaning the NWs are positioned directly during growth rather than depending on random alignment. In the first demonstration of this technique silicon (Si) NWs were grown on a silicon-on-insulator (SOI) substrate using a specially patterned gold (Au) catalyst and the VLS growth method [45, 46]. The need for a costly SOI substrate, difficulty of patterning Au and resulting metal contamination are some of the drawbacks of this method. Nanobridges (NBs) have also been demonstrated by growing ZnO NWs on a patterned ZnO seed layer (VS growth method) [32, 35]. Although there is no longer a need for a metal catalyst, this method still requires an SOI substrate, and reactive ion etching is required for trench formation, deposition, and patterning of the seed layer.

Very recently, Pelatt *et al.* demonstrated that the C-PR nucleation layer described by Cheng *et al* could be used to electrically-integrate NWs into NBs [17].

Their results showed that NBs could form three different ways: (i) the NWs can directly bridge from one C-PR pad to the other, (ii) two NWs can fuse together after growing from different C-PR pads, or (iii) one NW can grow from each pad and physically touch the other NW. The importance of the device structure, whether it is a single NW device or multiple NW device, and the effect of two physically touching NWs will be discussed further in Section 2.3.

2.3 Sensing Demonstrations

Bare and functionalized or coated nanowire sensors are reviewed to prepare readers for results presented in Chapter 4.

2.3.1 Bare Nanowires

Metal-oxide NWs have been used as sensors because of their high surface-to-volume ratio and sensitivity to gas species. A recent review by Ramgir *et al.* presents a representative review of sensors to date [10]. Generally, metal-oxide nanowires sensors are used to measure responses to NO_2 , NH_3 , O_2 , CO , H_2 , ethanol ($\text{C}_2\text{H}_5\text{OH}$) and acetone ($(\text{CH}_3)_2\text{CO}$). The work discussed in this section is for non-functionalized NW sensors which by nature are non-selective. Table 2.1 lists some of the results presented in literature related to this work.

Elevated operating temperatures are sometimes required to enhance the sensitivity of the device. The response of NW sensors is characterized by a change in

conductance/resistance based on modulation of carrier concentration by charged surface species adsorption. The response can be improved at higher temperature which facilitates surface adsorption and desorption. For ZnO NWs, the sensing mechanism is often described by the interaction of the NW surface with oxygen. When exposed to O_2 , oxygen will be adsorbed onto the NW surface and create a surface depletion region by capturing electrons near the surface [$O_2 (g) + e^- \rightarrow O_2^- (ads)$] and decreasing conductivity through the NW. The conductivity of the NW can be increased either by displacing surface oxygen or through the direct donation of an electron. For example, in the case of hydrogen sensing, the test gas can react with adsorbed surface oxygen [$2H_2 + O_2^- (ads) \rightarrow 2H_2O + e^-$] to donate an electron [47], thereby increasing the NW conductivity.

As suggested by Ahn *et al.* [11], the NB structure can be used to enhance device sensitivity. For example, in the case that NBs are formed, the junction between two physically connected NWs also experiences the effects of adsorbed and desorbed oxygen molecules, not just the surface of the NW. The potential barrier height at the junction between two nanowires is effectively raised with oxygen adsorption and a lower number of carriers have enough energy to overcome the barrier. There is a designation between devices that are based on multiple and single NWs because of added sensitivity arising from the NB structure and the fabrication and measurement challenges associated with isolating a single NW.

Zhang *et al.* explain that varied results in literature can be explained by the importance of doping-dependent sensing [53]. In ZnO systems, the inherent oxygen vacancies in nanostructures aid in device sensitivity because of the importance of

oxygen adsorption and desorption. Not only is doping used to modulate sensitivity, but the addition of functional or metallic materials to the surface can also improve device characteristics (see Section 2.3.2.).

2.3.2 Coated or Functionalized Nanowires

NW sensor response can be improved or altered by surface treatment. Tien *et al.* showed an increased response (approximately 5X) to H_2 when Pt clusters were sputtered on their ZnO NW sensor [65]. They point out that the Pt layer also increases the conductivity of the NWs by more than an order of magnitude. This increase is attributed to the sputtering process itself and possibly introducing more oxygen vacancies. Ramgir *et al.* describe that metallic coatings can either contribute as a chemical or an electronic catalyst [10]. For both types of catalysts, the sensitivity of the device is enhanced, but selective sensing has not been demonstrated. The distinction between the two categories is whether the enhancement of the sensor is from an indirect or direct effect. More specifically, when a metallic coating acts as a chemical catalyst, or sensitizer, the enhanced sensitivity of the device is said to be indirect. The enhancement comes from the catalyst's ability to increase the rate of surface chemical reactions. On the contrary, when a metal acts as an electronic sensitizer, it directly interacts with the semiconductor to enhance the sensitivity. In this case, metallic oxides are formed which can be reduced back to their metallic form in the presence of an inflammable gas [10]. Metal-enhanced sensors presented in the literature are listed in Table 2.2.

Table 2.1: Metal-oxide nanowire sensors

Nanowires Used	NW Structure	Temp ($^{\circ}\text{C}$)	Target	Ref
ZnO	Multiple	225	NO_2	[11]
ZnO	Multiple	RT-200	N_2 , air	[35]
ZnO	Multiple	200-250	H_2	[47]
ZnO	Single	RT	O_2	[48]
ZnO	Multiple	RT-250	H_2	[55]
ZnO	Multiple	180-300	$\text{C}_2\text{H}_5\text{OH}$	[56]
ZnO	Multiple	300	$\text{C}_2\text{H}_5\text{OH}$	[13]
ZnO	Multiple	200-400	$(\text{CH}_3)_2\text{CO}$	[14]
Ga₂O₃	Multiple	100-500	CO , O_2	[49]
In₂O₃	Multiple	400	NO_2 , $(\text{CH}_3)_2\text{CO}$	[50]
In₂O₃	Multiple	150	NO_x	[51]
In₂O₃	Single, Multiple	RT	NO_2	[52]
In₂O₃	Single	RT	NH_3	[53]
In₂O₃	Multiple	RT	$\text{C}_2\text{H}_5\text{OH}$	[54]
SnO₂	Multiple	200	NO_2	[4]
SnO₂	Single	180	H_2O vapor	[57]
SnO₂	Multiple	200	H_2	[58]
SnO₂	Multiple	220-320	CO , O_2	[59]
SnO₂	Multiple	200-450	$(\text{CH}_3)_2\text{CO}$	[60]
WO₃	Multiple	150	NO_2	[61]
WO₃	Multiple	RT	NO_2	[62]
TiO₂	Single	100	CO	[63]
TiO₂	Single	RT	H_2	[64]

Table 2.2: Metal-enhanced nanowire sensors

Nanowires Used	NW Structure	Temp ($^{\circ}\text{C}$)	Target	Ref
ZnO-Pt	Single	RT	H ₂	[65]
ZnO-Au	Multiple	250-350	CO	[66]
ZnO-Pd	Multiple	170-230	C ₂ H ₅ OH	[67]

There are limited reports on the effects of non-metallic coatings on ZnO NB sensing characteristics. Lao *et al.* report on the effects of polymer surface-functionalization on the UV response of ZnO nanobelts. Before coating the device with the polymer of choice, a poly(diallyldimethylammonium chloride) (PDADMAC) polymer was first attached to a single nanobelt-based device. The PDADMAC is positively charged, so the attachment of various negatively charged polymer coatings was achieved using electrostatic assembly. They provide UV illumination results for a nanobelt coated with PDADMAC/polystyrene sulfate (PDADMAC/PSS) and PDADMAC/poly(styrene-co-maleic acid) (PDADMAC/PS-co-Mac) in addition to the response of an uncoated nanobelt. For both polymer coatings, the UV response was larger than that of an uncoated nanobridge device. The authors attribute the enhancement to two separate mechanisms one for each polymer coating system. For the PDADMAC/PS-co-Mac, Lao *et al.* suggest that the PDADMAC is trapping free electrons (since it is positively charged) and upon UV illumination these electrons will trap holes created through photogeneration which will reduce the electron-hole recombination within the NW itself. For the PDADMAC/PSS, Lao *et al.* postulate that the PDADMAC layer does not cover

the entire ZnO NW, but that the PSS layer also directly interacts with the ZnO. The peak absorption for PSS is approximately 260 nm, very close to the 280 nm UV source used in their experiment. It is suggested that the PSS provides an intermediate “hopping” state for electrons which increases the number of electron-hole pairs. This mechanism, combined with the hole-trapping of PDADMAC, is used to explain the increase in the photoconductance. No gas sensing measurements were performed in this study [68].

Song *et al.* used PMMA (polymethyl methacrylate) as a passivation layer for their single ZnO NW based transistor. For their application, device sensitivity to surface oxygen was a concern. When the ZnO NW device was unpassivated, oxygen-rich environments were found to impact the carrier concentration, carrier mobility, and threshold voltage undesirably. However, when the ZnO NW device was passivated with PMMA, the device performance remained consistent regardless of the environment [69]. In their work, the PMMA was purely used as a passivation layer and the ZnO NW device was not used as a sensor, so some preliminary work would be needed to determine if the PMMA layer is compatible with sensing applications. Additionally, the PMMA layer would still need to be functionalized to facilitate selective sensing.

Chapter 3 – Methods and Materials

Methods of device fabrication, processing, and testing are presented in this chapter. Processing consists of coating the nanowires with parylene-A, while testing consists of evaluating the electrical performance of each sample.

3.1 Base Nanobridge Device Fabrication

Fig. 3.1 shows the fabrication procedure for the base device. First a 300 nm thick insulating layer of wet oxide was grown on silicon, followed by photoresist (PR) deposition and direct lithographic patterning (Shipley 1818). Next, the patterned PR was carbonized at a pressure of 1.4 Torr in N_2 at 900 °C. Molybdenum (Mo) is sputtered from a 3" target at 100 W and a pressure of 3.5 mTorr and patterned using liftoff. The Mo layer is used to simultaneously decrease contact resistance and prevent ZnO NW growth on the contact area [17].

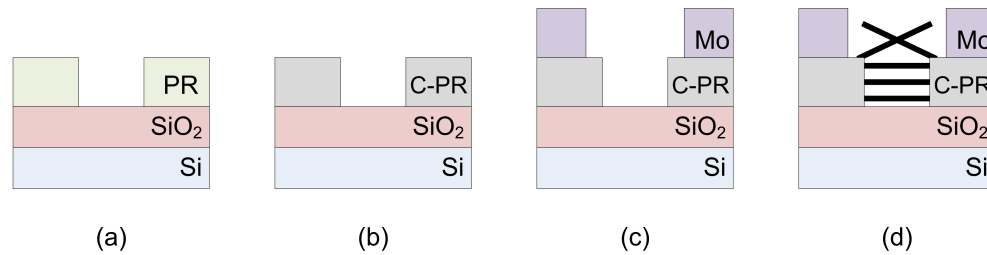


Figure 3.1: Processing steps for ZnO nanobridge devices.

Next, vapor-solid growth of ZnO nanowires (NWs) was performed using a 1:1 ratio of ZnO and graphite powders. In carbothermal reduction the graphite is used to decrease the temperature needed for evaporation as described in work by Yao *et al.* [33]. The ZnO/graphite precursor mixture was either blended by hand or using a SWECO vibratory mill. As discussed in Chapter 4, vibratory milling was used to improve NW growth. The growth process was performed using a two zone Carbolite CVD tube furnace. The precursor mixture was placed in the first zone which is set at 920 °C; the second zone temperature was set at 500 °C. Fig. 3.2 shows the ZnO NW growth set-up and the two heated zones. 150 sccm of N₂ is used to carry the evaporated precursor down to the growth substrate which was placed in the furnace at approximately 770 °C for 30-45 minutes. An O₂ injection tube (1-5 sccm) was positioned at the end of the precursor boat and was used to aid in the formation of ZnO nanobridges.

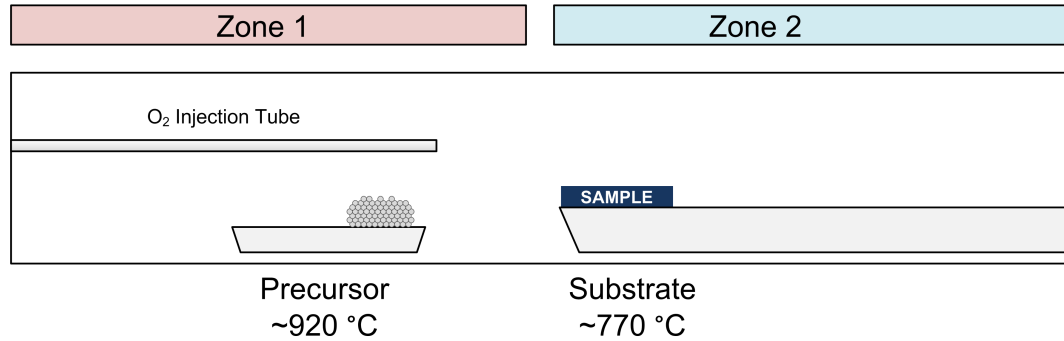


Figure 3.2: ZnO nanowire growth set-up.

3.2 Protection of ZnO Nanowires

Parylene-A coating was performed using the same CVD tube furnace as carbonization and ZnO NW growth. Note that each process (carbonization, NW growth, and parylene-A deposition) has a dedicated quartz tube to avoid cross-contamination. As mentioned in Chapter 2, the “A” designates the amine functional group. For comparison, different types of parylenes are shown in Fig. 3.3. Parylene-A is manufactured as a dimer, so, as shown in Fig. 3.4, after vaporization at 150 °C the parylene-A must be pyrolyzed (broken into a monomer) at 690 °C. To ensure parylene-A deposition, a cooling rod is used to keep the sample at room temperature.

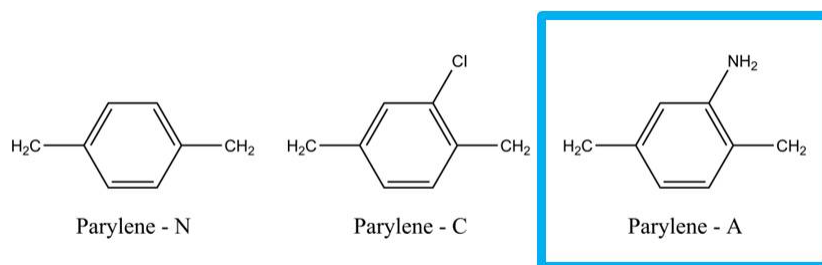


Figure 3.3: Common types of parylene.

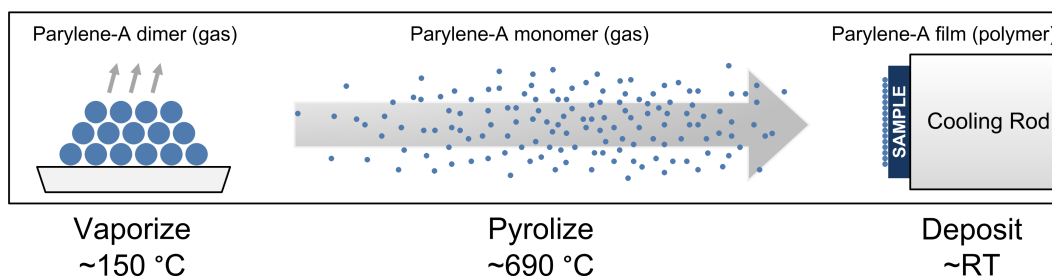


Figure 3.4: CVD process used for parylene-A coating.

The hydrophobicity of a blanket of ZnO NWs before and after parylene-A coating was evaluated using an FTÅ 135 Contact Angle and Video Analysis system. To further determine the efficacy of the coating, dark field microscopy was used to image uncoated and coated ZnO nanobridge samples after various soaking times in deionized (DI) water.

3.3 Electrical Characterization and Gas Sensing

Electrical characterization was performed in a dark box using an Agilent 4155C semiconductor parameter analyzer (SPA). The UV response of the devices was characterized with a 254 nm, 18.4 W Mineralight lamp (designated as UV1). Gas sensing was performed using an Agilent B1500 semiconductor device analyzer (SDA) and a NorECs ProboStat. A photo of the set-up used for sensing O₂, H₂O, CO and N₂/H₂ is shown in Fig. 3.5. Nitrogen was used to purge the high temperature measurement cell between measurements. Also shown in Fig. 3.5 is the nitrogen bubbler which nitrogen was flowed through to create the wet N₂ used for H₂O sensing. Mass flow controllers (MFCs) used to control the flow rate of nitrogen, carbon monoxide, oxygen and forming gas. A schematic diagram of the gas sensing set-up including gas inlets and outlets is shown in Fig. 3.6.

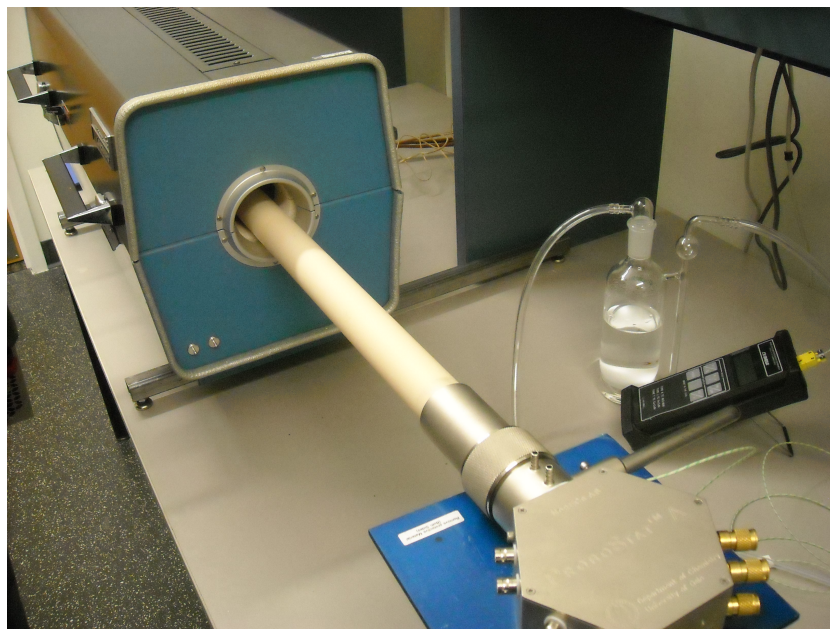


Figure 3.5: The NorECs ProboStat used for gas sensing measurements.

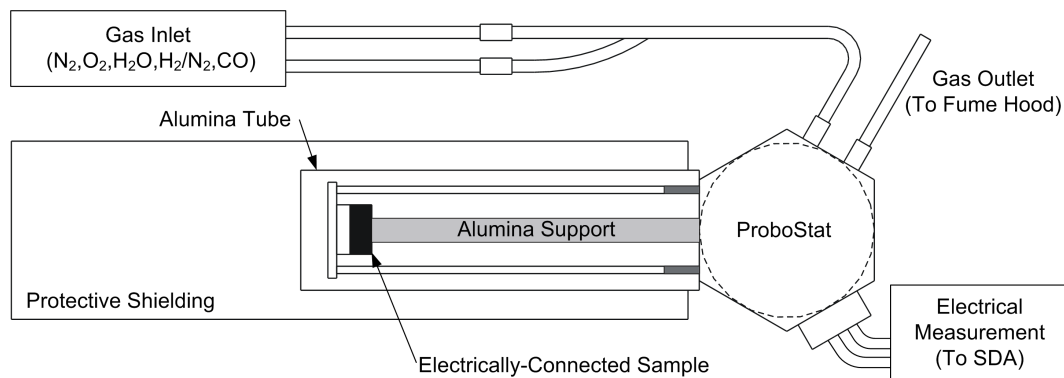


Figure 3.6: Schematic diagram of the gas sensing measurement set-up.

Fig. 3.7 shows a sample inside of the NorECs ProboStat. In the image on the left-hand side, there are two wires used to connect to the sample. A third wire can be seen behind the alumina sample holder. A fourth wire is actually present, but not visible in this image. These two wires are used to electrically connect an in-situ InGaN for use during the measurement. Fig. 3.8 shows wavelength characteristics of the LED measured with an optical spectrometer, the maximum wavelength observed was approximately 406 nm with a full width at half maximum (FWHM) of about 13 nm (designated as UV2). During the spectrometer and gas sensing measurements 3.3 V was applied across the LED and 20 mA compliance were used.

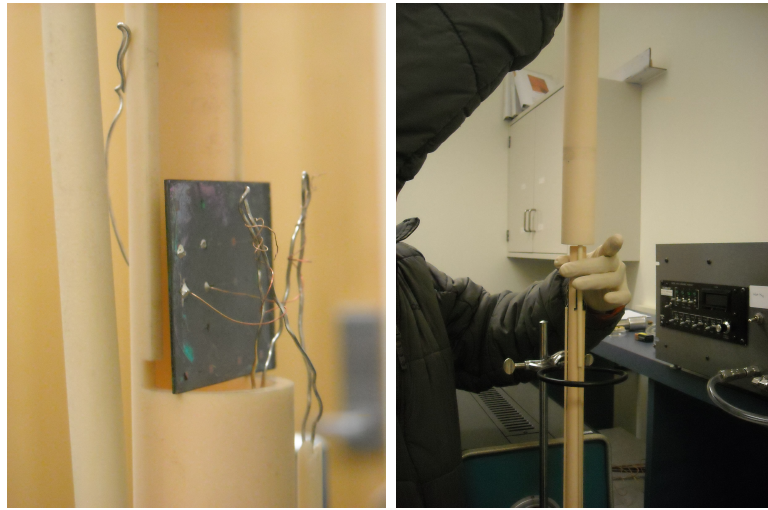


Figure 3.7: A sample loaded in the NorECs ProboStat showing electrical connections and the inside of the probostat.

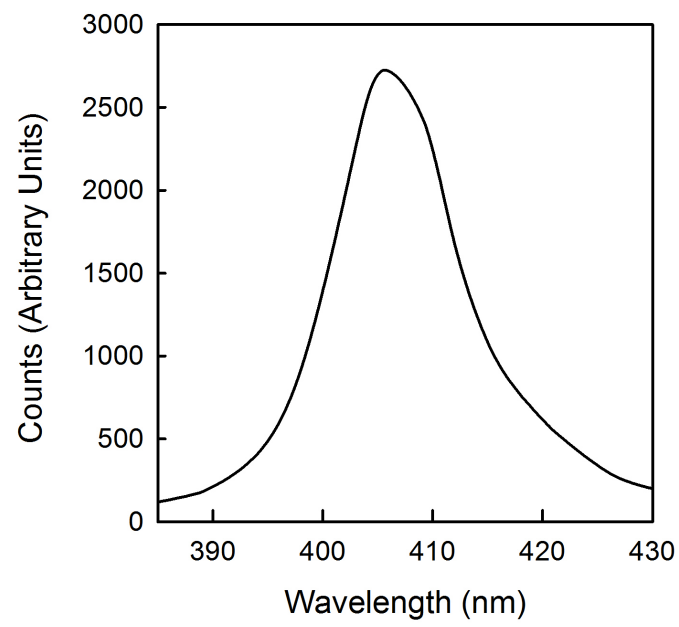


Figure 3.8: The resulting characteristics of the InGaN used for in-situ UV during gas measurements obtained using optical spectroscopy.

Chapter 4 – Results and Discussion

In this chapter, results on the ZnO nanowire (NW) growth and nanobridge device optimization are presented, followed by UV and gas phase sensing with and without parylene-A.

4.1 Growth Optimization

Over the course of our earlier experiments, variation in NW density and morphology was observed. The precursor temperature and the O₂ injection flow rates (see Fig. 3.2) were adjusted to optimize repeatability between runs and to improve NW uniformity across the sample. The resulting NWs were examined using scanning electron microscopy (SEM). For all SEM images, a FEI Quanta was used at a working distance of 10 mm and accelerating voltage of 20 kV.

4.1.1 Effect of Growth Temperature

In order to determine the impact of the precursor temperature on NW growth, the precursor temperature was varied from 920-930 °C. This temperature range was chosen because at temperatures above 930 °C selective growth was lost, meaning that ZnO NWs would form on the SiO₂, as well as the C-PR. When temperatures below 920 °C were used, NWs would not form. In Fig. 4.1 the nanobridges (NBs)

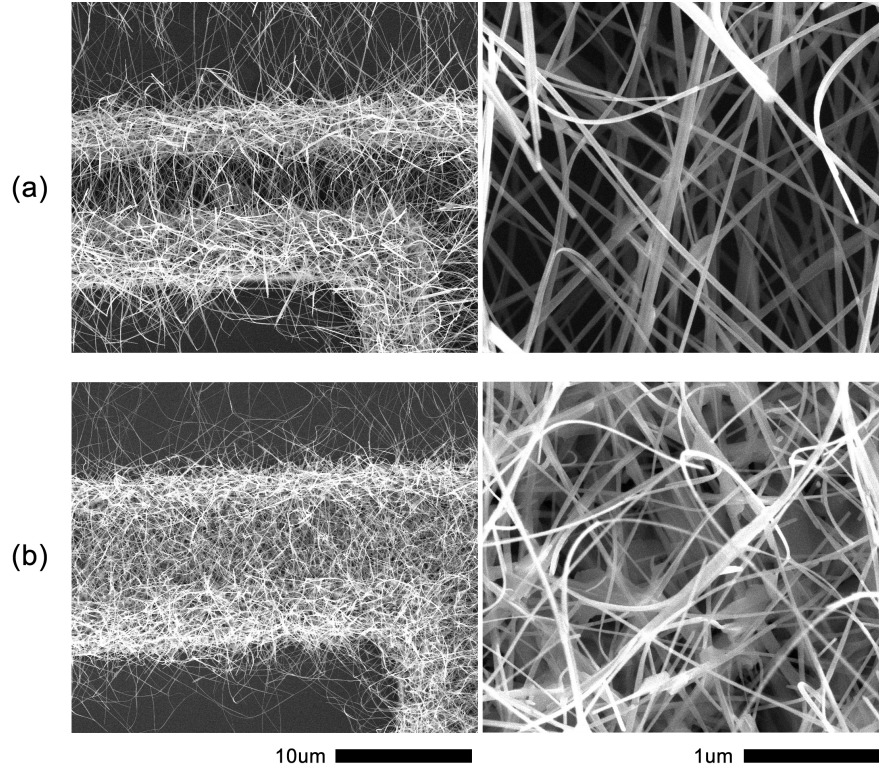


Figure 4.1: SEM images of ZnO NBs grown for 40 minutes using an O₂ flow rate of 3 sccm, 150 sccm of N₂ carrier gas, pressure of 1.4 Torr, and a precursor temperature of (a) 925 °C and (b) 930 °C.

with a precursor temperature of (a) 925 °C and (b) 930 °C are pictured. The NW growth looked very similar for 920 and 925 °C growth (only 925 °C pictured), NWs did not grow at 915 °C. Note that the high resolution image in Fig. 4.1(b) not only shows ZnO NBs, but also possibly ZnO grains under the NBs. These ZnO grains could contribute to a higher current through the device without contributing to the sensing capabilities of the ZnO NBs.

4.1.2 O₂ Injection

The O₂ injection tube shown in Fig. 3.2 is used to control oxygen required for ZnO NW growth. Fig. 4.2 shows NBs grown using an O₂ flow rate of (a) 5 sccm, (b) 3 sccm and (c) 1sccm. The best results for our work were obtained at 1 sccm. The lower density of the NWs in this sample is an advantage for sensing. The chance that NWs could shield other NWs in our 3D nanobridge device, or that NWs could contribute to the base device current but not to the device gas sensitivity is reduced with a lower density NB. When a flow rate of 1 sccm is used, the diameter of the NWs is also more consistent and no thicker NWs or nanoribbons (NRs) are formed. Thicker NWs are undesirable because as shown by Fan *et al.*, thicker NWs are less sensitive to test gases (i.e. O₂) [70].

4.1.3 Vibratory Milling

Originally a mortar and pestle were used to mix the ZnO powder and graphite precursor. Vibratory milling was investigated as an alternate way to mix the precursors. The resulting growths for both methods at 930 °C, 5 sccm O₂, 150 sccm of N₂ carrier gas, 40 minute growth time, and a pressure of 10 Torr are shown in Fig. 4.3. Vibratory milling was found to not only extend the range of growth parameters where selective growth of NWs was possible, but at the same settings the NWs were thinner and more uniform. Note that in Fig. 4.3(a) the missing ZnO growth is from a scratch on the sample where C-PR was removed from the substrate.

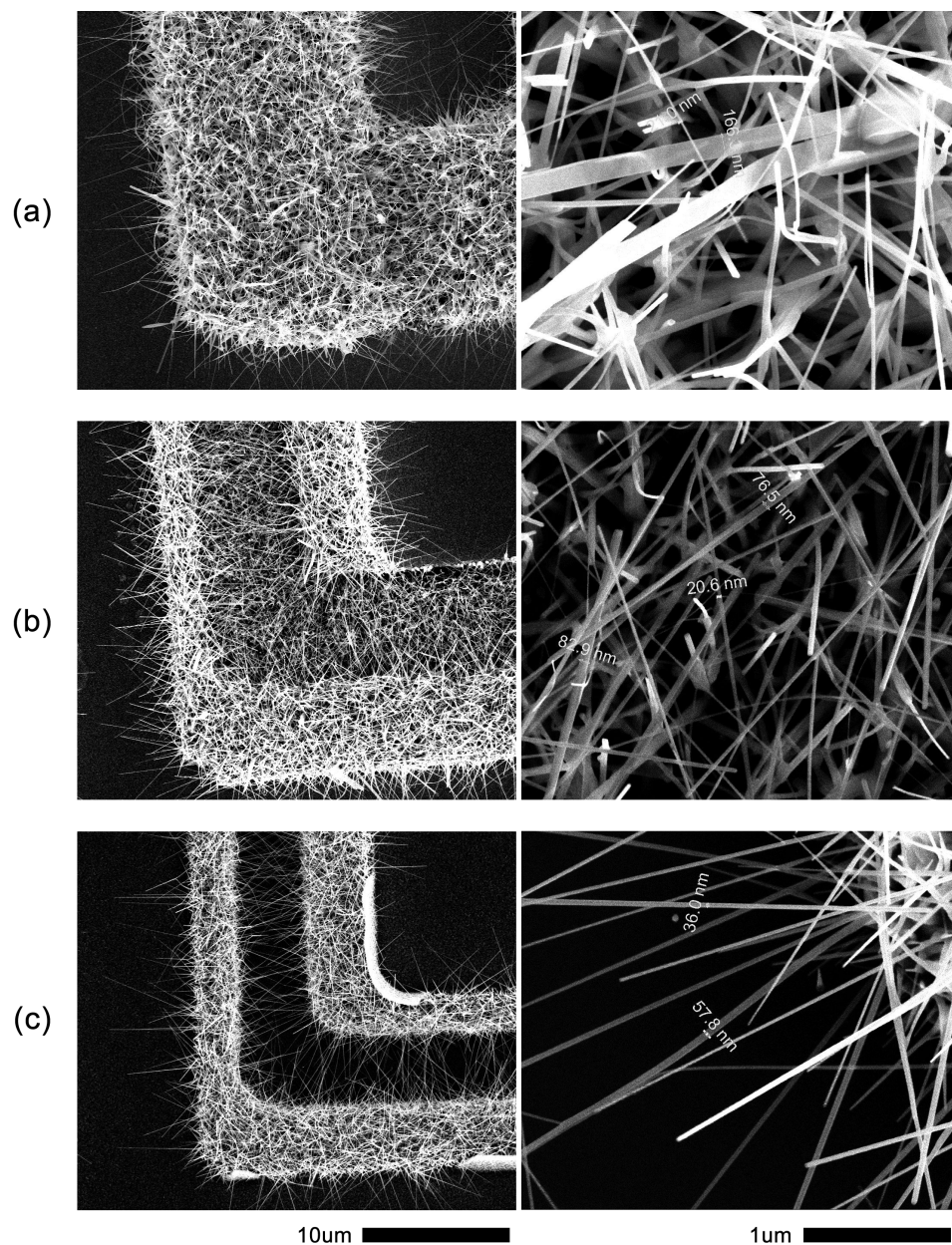


Figure 4.2: SEM images of ZnO NBs grown for 40 minutes using 150 sccm of N_2 carrier gas, a pressure of 1.4 Torr, precursor temperature of 920 $^{\circ}C$ and an O_2 injection flow rate of (a) 5 sccm, (b) 3 sccm, and (c) 1 sccm.

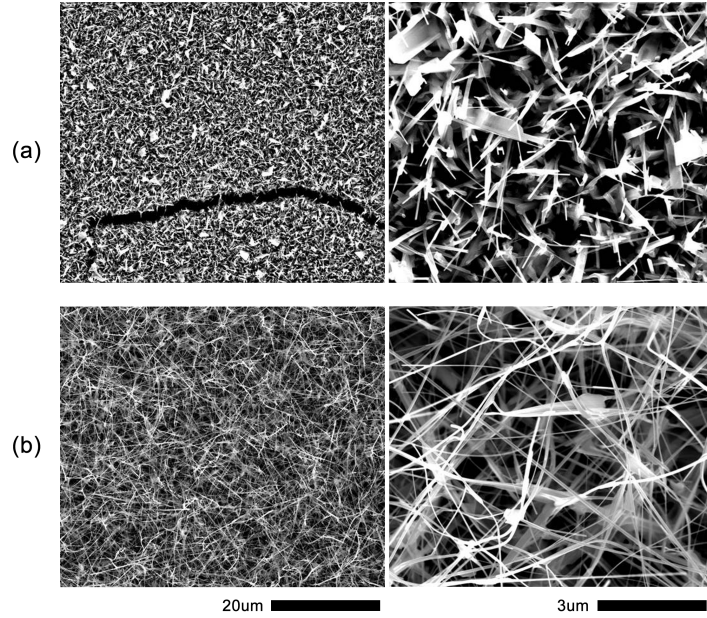


Figure 4.3: SEM images of ZnO NBs grown for 40 minutes using a precursor temperature of 930 °C, 5 sccm O₂, 150 sccm of N₂ carrier gas, and a pressure of 10 Torr utilizing (a) mortar and pestel mixing, or (b) vibratory milling to mix the precursor.

The optimal growth conditions are: a precursor temperature of 920 °C, a substrate temperature of approximately 770 °C, an O₂ injection flow rate of 1 sccm, 150 sccm of N₂ carrier gas, and a 40 minute growth time at a pressure of 1.4 Torr. As discussed below, using these growth parameters, devices had a larger UV response and were more sensitive to test gases. Note that for the studies on the effect of temperature and O₂ injection, the precursor was mixed using a mortar and pestel, rather than vibratory milling. The electrical measurements presented are for NBs grown using the optimal conditions and vibratory milling unless noted otherwise.

4.2 Base Device

ZnO nanobridge (NB) device designs were refined to increase the device response and improve device repeatability. Devices were characterized using I-V measurements, UV illumination and gas sensing.

4.2.1 Device Design and Refinements

The original design for ZnO NBs is shown in Fig. 4.4(a). The Mo layer was added to decrease resistivity because although Cheng *et al.* reported that as-carbonized C-PR had resistivity similar to indium tin oxide (ITO) [16], Pelatt *et al.* showed an increase in resistivity after NW growth [17]. The addition of the Mo layer decreased the sheet resistance of the contact by three orders of magnitude [17]. Shown in Fig. 4.4(b), interdigitated fingers were added and the Mo metallization was extended to decrease the effect of leakage through the contact pads and limit ZnO NW growth to the NB region. In both schematics, the dark regions represent C-PR and the lighter regions represent the Mo layer. Fig. 4.5 shows the schematic cross-section of a device and the labels for the drain (D), gate (G), and source (S).

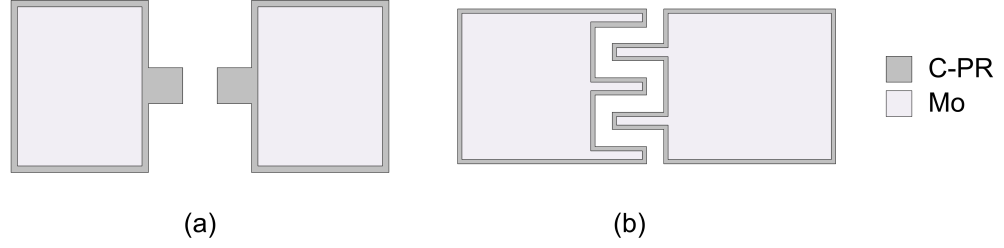


Figure 4.4: Top-down schematic of (a) original and (b) revised ZnO NB devices showing C-PR and Mo regions.

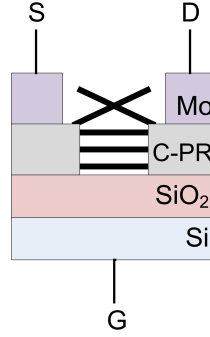


Figure 4.5: Device schematic cross-section showing the NB drain (D), gate (G), and source (S).

The performance of the “old” and “new” devices were compared using UV response measurements. The UV excitation used in these experiments was UV1 (see Chapter 3). For the results presented in Fig. 4.6, the gap between the C-PR fingers is $5\text{ }\mu\text{m}$, $V_{DS} = 3\text{ V}$, and the gate was left floating. Because of the increased active device area, the effect of leakage current through the large contact pads is lower and device sensitivity to UV illumination is enhanced.

When a ZnO NB device is in the dark, O_2 is adsorbed on the surface of the NW. As described in Section 2.3.1 the adsorption of oxygen [$\text{O}_2(\text{g}) + \text{e}^- \rightarrow \text{O}_2^-(\text{ads})$]

and capture of electrons near the surface creates a surface depletion region which decreases the NW conductivity. Upon UV exposure electron-hole pairs are generated within the NW nearly instantaneously increasing the current through the NWs. The newly-created holes drift towards the surface of the NWs and discharge the oxygen [$\text{O}_2 (\text{ads}) + \text{h}^+ \rightarrow \text{O}_2 (\text{g})$]. The electrons that were originally captured by the oxygen are now free and further increase the NW conductivity. When the UV source is removed excess electrons and holes recombine forthwith resulting in an immediate decrease in conductivity. However, oxygen readsorption and further decrease of conductivity by recreating the depletion region is a slower process which can lead to an increase in decay time.

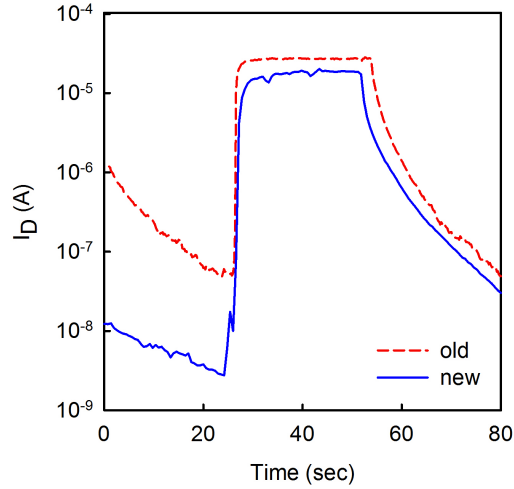


Figure 4.6: Plot of UV response for “old” and “new” design 5 μm gap devices where $V_{DS} = 3$ V, and the gate was left floating. The old device structure is shown in Fig. 4.8(a) and the new device structure is shown in Fig. 4.8(b).

Although sensitivity to UV was improved with the first design revision, the dark current between devices could still vary over an order of magnitude between samples because of NW growth variation. A second design revision used a series resistance design to address the issues of device performance and repeatability. An image showing the top-down view of the series resistance device (SRD) is shown in Fig. 4.7.

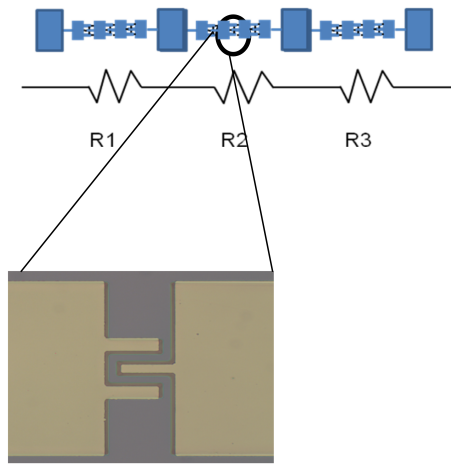


Figure 4.7: Device revision: Series resistance design (SRD).

In Section 4.1, a discussion of growth process optimization was presented. In that section it was pointed out that optimal devices had sparsely grown thin NWs. A device with a lower NW density will have a higher resistance. Since the highest resistance device dominates the overall behavior of resistors in series, device performance as well as repeatability was enhanced by using the SRD. Fig. 4.8 shows the I-V measurement and UV response of two $5\text{ }\mu\text{m}$ gap SRD NB devices, and the successful improvement in device repeatability. The results presented are for two separate samples, measured from R1 to R3 (the entire SRD strand).

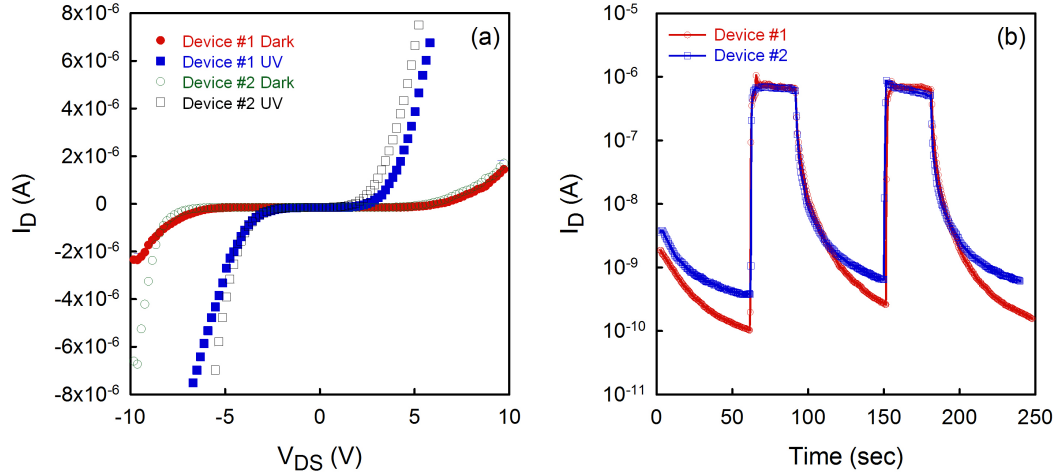


Figure 4.8: Plot of (a) I_D vs V_{DS} in the dark and under UV1 illumination and (b) I_D over time when exposed to 30 seconds of UV1 with $V_{DS} = 3$ V for two $5 \mu\text{m}$ gap SRD NB devices.

The I-V measurements for two $5 \mu\text{m}$ gap SRD NB devices measured in the dark and under UV1 illumination is presented in Fig. 4.8(a). The shape of the data is characteristic of a double Schottky barrier. As described in Chapter 2, when two NWs physically touch, adsorbed oxygen bends the energy band upward resulting in a double Schottky barrier. When NB devices are formed, there are different types of connections between the C-PR pads. NWs can either (i) directly connect one pad to the other with a single NW, (ii) grow from separate pads and fuse together, or (iii) physically touch after growing from two separate pads [18]. In a previous report Huang et al. demonstrated that type (ii) is the most dominant connection demonstrated by the device behavior observed in Fig. 4.8(a) [18].

Fig. 4.8(b) shows the UV1 response of two 5 μm gap SRD NB devices, from two different growths, showing the improvement of device repeatability.

One concern with the data presented in Fig. 4.6 and Fig. 4.8 is the long recovery time, or the “tail” after the UV source has been removed. The decay time (the time it takes for I_D to decrease to 10 % of its maximum value) for our devices are comparable to results presented in literature (see Table 4.1). However, the time it takes for the device to fully return to its initial dark current value is not always reported. A N_2 cleaning, where a N_2 gun was used to clean the device area for one minute, after device growth was found to improve the recovery time. A comparison of as-prepared and N_2 cleaned UV response measurements are presented in Fig. 4.9. After the N_2 clean, the dark current in the device is decreased. This could be attributed to additional loose ZnO particulates or NWs not directly connected to the C-PR contributing to a higher dark current in an uncleaned device. The use of a N_2 clean to remove these particulates also decreases device instability (changes in device performance between measurements) and the total response time.

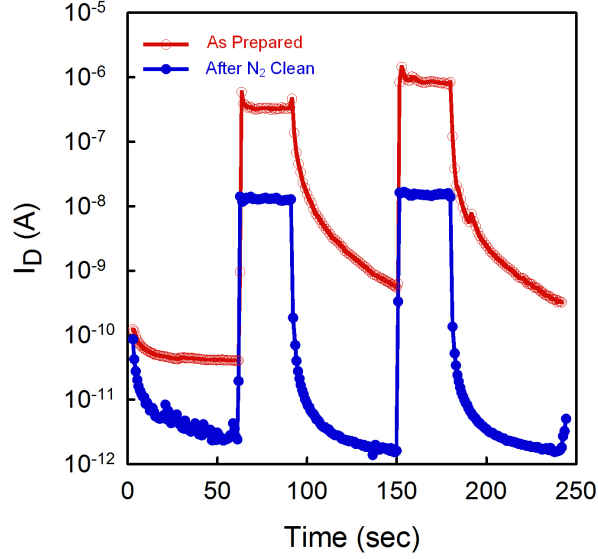


Figure 4.9: Plot of I_D over time for an as prepared and a N_2 cleaned $5\ \mu\text{m}$ gap SRD NB device exposed to 30 seconds of UV1 with $V_{DS} = 3\ \text{V}$.

Fig. 4.10 shows the gas sensing response of two $5\ \mu\text{m}$ gap ZnO NB devices prepared at a precursor temperature of either $925\ ^\circ\text{C}$ or $930\ ^\circ\text{C}$ with an O_2 injection flow rate of 3 sscm. SEM images of the devices are shown in Fig. 4.1. The measurements were made within a closed gas flow chamber with $V_{DS} = 3\ \text{V}$ and the gate left floating. The data shown is the normalized current for the device, where the measured current is divided by the current through the device when stabilized under N_2 . The device made with a precursor temperature of $925\ ^\circ\text{C}$ has a higher sensitivity to both H_2O and O_2 . The NW growth at a $930\ ^\circ\text{C}$ precursor temperature was found to be more dense than at $925\ ^\circ\text{C}$. As discussed in Section 4.1, the higher NW density and formation of thicker NWs and NRs contributed to a lower gas response for the sample made using a precursor temperature of $930\ ^\circ\text{C}$.

Although a N_2 purge was included in between measurements, the order of the measurements can impact the results. This effect was also seen and reported by Huang *et al.* [18]. For the data in Fig. 4.10, the response of the 925 °C precursor temperature sample to H_2O is uncharacteristic and instead of seeing a more gradual increase in conductivity the sensor response is considerably faster. It is possible that although the N_2 purge was included, more O_2 was adsorbed to the NW surface increasing the observable change in NW conductivity when H_2O either replaces surface O_2 or donates an electron.

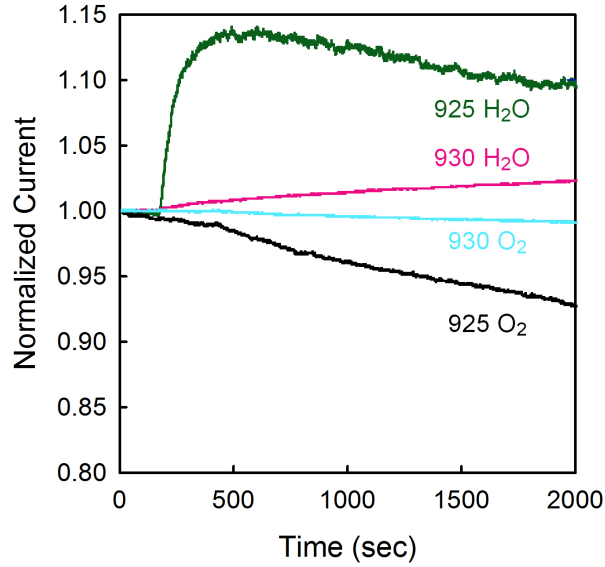


Figure 4.10: Plot of O_2 and H_2O sensing for 5 μm gap SRD NB devices with precursor temperatures of 925 °C and 930 °C used during growth.

As discussed earlier and shown in Fig. 4.6, the device response was improved when the influence of device leakage was reduced. To further enhance the UV sensitivity the SiO_2/Si base substrate was replaced with a glass substrate because

the thick glass was expected to be a better insulator than the steam-grown SiO_2 . The UV response for a $5\ \mu\text{m}$ gap ZnO NB on glass is shown in Fig. 4.11. Table 4.1 presents the UV sensitivity results obtained during the course of this thesis and published literature values. Please note that the inclusion of the “<” in the values reported for rise and decay time is because the measurement interval used was 400 ms. It is difficult to make direct comparisons due to differences in λ , the NW current, and device structure. However, the magnitude of our UV response is the largest reported value reported to date without the use of an applied gate voltage, V_G . As discussed by Huang *et al.* [18], the use of a negative back-gate voltage can be used to enhance the I_{ON}/I_{OFF} ratio, which is why there is a note in Table 4.1 if a gate bias is used.

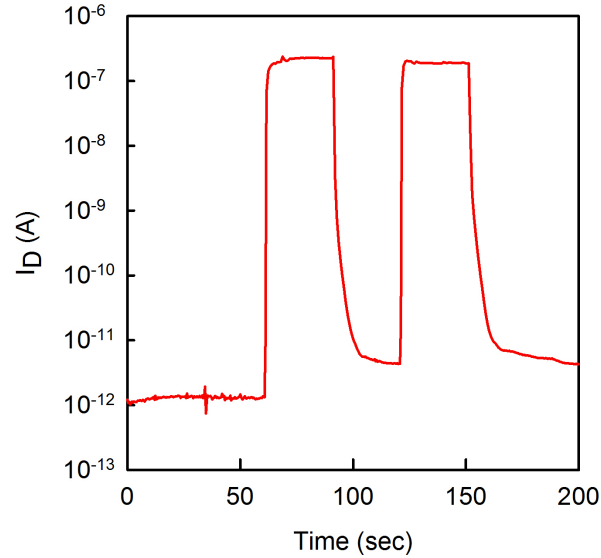


Figure 4.11: Plot of I_D over time when exposed to 30 seconds of UV1 with $V_{DS} = 3\ \text{V}$ for a $5\ \mu\text{m}$ gap SRD NB device on glass substrate.

Table 4.1: UV response of ZnO NWs

Rise Time (s)	Decay Time (s)	I_{ON}/I_{OFF}	λ	Ref	Notes
<u>This Work</u>					
<0.4	<1.2	2×10^3	254 nm		SRD #1
<0.4	<1.2	10^3	254 nm		SRD #2
		2×10^5	254 nm		SRD on glass
<u>Literature</u>					
1.2	4.4	400-1000	254 nm	[18]	V_G bias applied
—	47	10^6	365 nm	[71]	V_G bias applied
0.7	1.4	10^{-10}	350 nm	[72]	
0.6	6	1500	365 nm	[73]	
4	30	10	350 nm	[74]	
0.4×10^{-3}	0.36×10^{-3}	1.15	370 nm	[75]	
1	180	10^2	-	[35]	

4.3 Parylene-A Coating

A CVD process for parylene-A was developed to act as a protection and activation layer for further functionalizing the ZnO NWs. Physical and electrical characterization of the parylene-A films as well as their effect on ZnO NB performance are presented.

4.3.1 Physical Characterization

In our earlier work, biotin was successfully attached to ZnO NWs as described in detail by Mason *et al.* [23]. Images of patterned ZnO NW growth on Si/SiO₂ modified with biotin and labeled with FITC conjugated streptavidin are shown in Fig. 4.12. However, when exposed to DI water, the nanowires dissolve as shown in Fig. 4.13. Conformal parylene-A coatings were developed and were used to successfully protect ZnO NWs. Contact angles of a DI water droplet on a film of ZnO NWs before and after parylene-A coating are shown in Fig. 4.14. Dark field microscope images in Fig. 4.15 show that parylene-coated NWs remain unharmed after 24 hours in DI water.

To measure the thickness of the parylene-A, a polydimethylsiloxane (PDMS) mask was attached to a section of a glass sample which was then coated with parylene-A. After the coating, the PDMS mask was removed and atomic force microscopy (AFM) was used to measure the step height. The parylene-A layer was approximately 20 nm thick and had an root mean square (rms) roughness of 2 nm. For reference, the rms roughness of the glass sample was 1.5 nm.

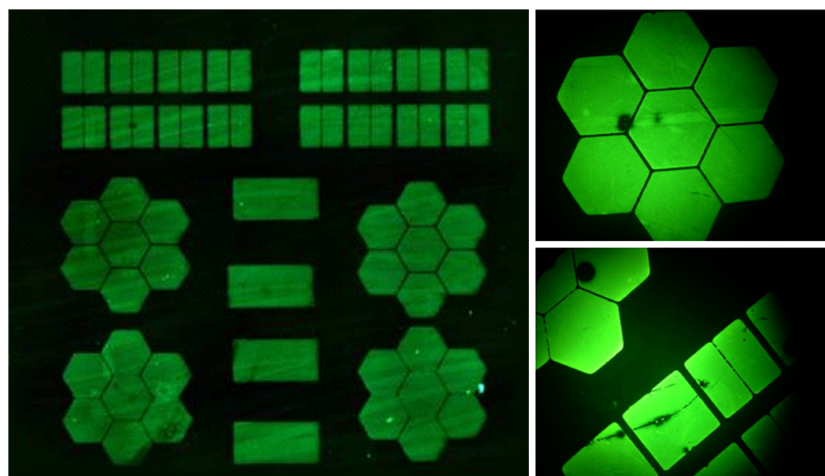


Figure 4.12: Fluorescence microscopy images of ZnO NWs modified with biotin and FITC conjugated streptavidin.

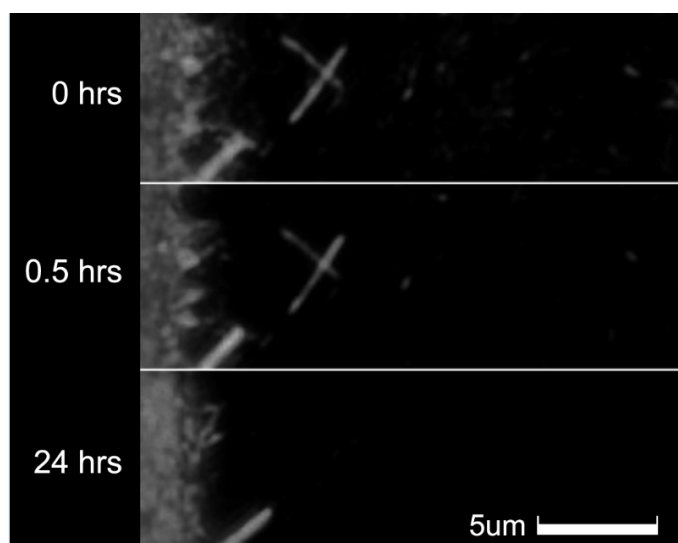


Figure 4.13: Dark field microscope images as a function of time for a ZnO NB device coated with biotin left continuously in DI water.

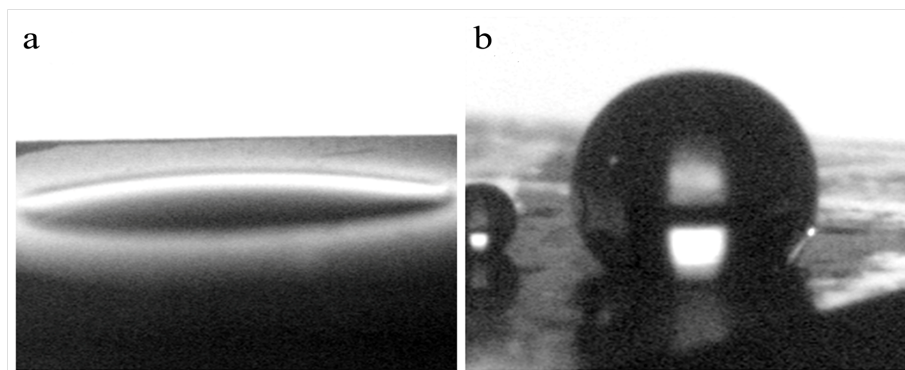


Figure 4.14: Contact angle measurements on ZnO NWs (a) before and (b) after parylene-A coating.

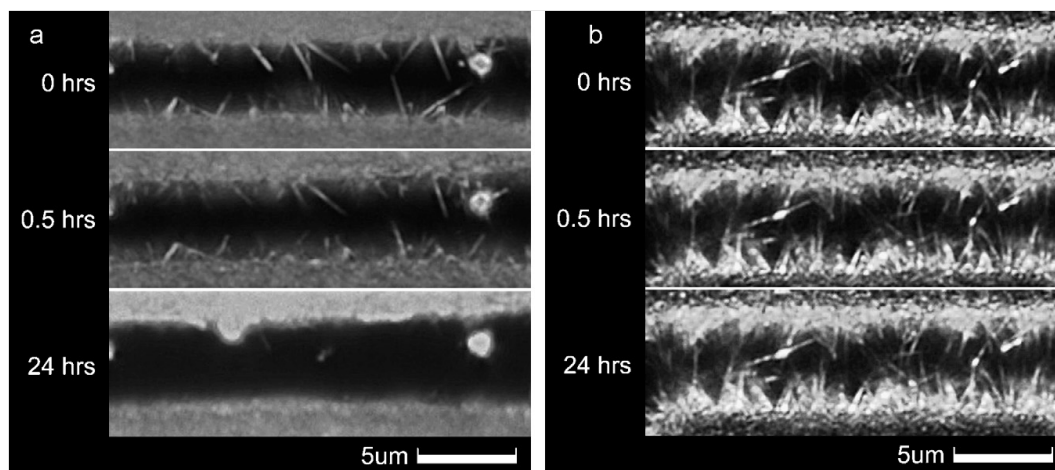


Figure 4.15: Darkfield microscope images as a function of time for a ZnO NB device submerged in DI water (a) before and (b) after parylene-A coating.

4.3.2 Electrical Characterization and Gas Sensing

In Chapter 3, general results for ZnO NW sensors were presented, and although several reports discuss the electrical properties of ZnO NW sensors, the effect of a non-covalently bound polymer passivation layer on gas sensing has not been investigated. The impact of the added parylene-A layer on I-V behavior, UV sensitivity, and response to O_2 and H_2O was recently reported by Mason *et al.* [23].

Fig. 4.16 shows the I-V characteristics and UV response for a 5 μm device with a floating gate before and after coating with parylene-A. As described in Chapter 2, the dominate type of connection in these NB structures is the physical touching of two wires. When these connections are created, a double Schottky barrier is formed between the two NWs which dominates the overall current transport. Adsorbed O_2^- results in upward band bending at this junction, reducing the current. In Fig. 4.16(a) it appears that the Schottky behavior of the device is more pronounced before the parylene-A coating. This could be explained by a reduction in surface sites available for O_2 adsorption when the device is coated with parylene-A.

Fig. 4.16(b) shows the UV response of the same NB before and after parylene-A coating under UV1 illumination. Note that these results are presented on a linear scale. Although the photocurrent is higher for the parylene-A coated device (compared to the uncoated device), the dark current is higher as well.

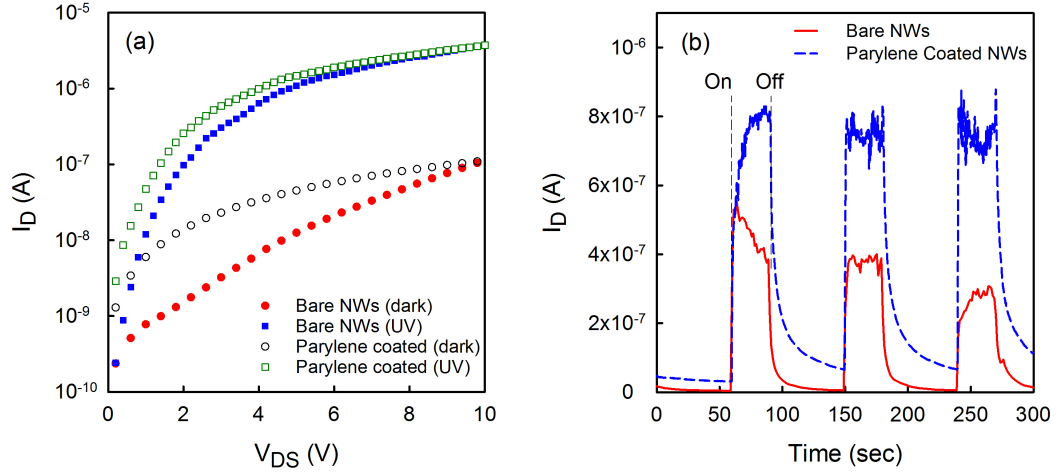


Figure 4.16: Plot of (a) I_D vs V_{DS} in the dark and under UV illumination and (b) I_D vs time when periodically exposed to 30 seconds of UV with $V_{DS} = 3$ V for a $5 \mu\text{m}$ gap SRD NB device on a Si/SiO₂ substrate.

Upon UV exposure, I_D for the uncoated device increases 100x whereas the parylene-A coated device only experiences a 45x increase in I_D . The response to UV illumination is considerably smaller than our results presented in Table 4.1. The sample measured and presented in this figure was grown using an O₂ flow rate of 3 sccm instead of 1 sccm (with the rest of the conditions at their optimal setting including vibratory milling). NWs grown using a higher O₂ flow rate were more dense and, as discussed in Section 4.1.2, the higher NW density and 3D structure of our NB device could contribute to a lower UV response because of NWs shielding other NWs. As described in Section 4.2.1, the UV response of ZnO NWs is not only caused by the direct photogeneration of carriers, but also surface interactions with ambient, particularly the adsorption and desorption of oxygen. In

addition to the aforementioned change in I_D - V_{DS} behavior, a decrease in available oxygen adsorption sites could also explain the higher dark current observed after parylene-A coating.

The increase in the photocurrent after parylene-A coating could be explained by a decrease in available adsorption sites for O_2 and H_2O . Li *et al.* discuss competitive surface effects of O_2 and H_2O and resulting differences in the UV response from changing the relative humidity used during the measurement. According to their report, H_2O molecules adsorbed on the NW surface will attract electrons and holes, decreasing the carrier concentration and photocurrent [76].

Fig. 4.17 shows the response of a parylene-A coated $5\ \mu\text{m}$ gap SRD NB device on a Si/SiO₂ substrate to both O_2 and H_2O (wet N₂). For these experiments, the total flow rate was kept at 200 sccm and the response to different partial pressures of the test gas was measured. To clarify, when 50 sccm of O_2 is used, 150 sccm of N₂ is flowed through the system and when 5 sccm of O_2 is used, 195 sccm of N₂ is flowed through the system. As described earlier, the adsorption of O_2^- on the surface of the ZnO NWs causes a surface depletion region and a decrease in total current flow. With a higher partial pressure of O_2 the response is faster because the surface can be more quickly saturated with oxygen. The current within the NW can be increased when the sensor is exposed to H_2O . The increased conductivity can either be attributed to the H_2O displacing an adsorbed oxygen or the direct donation of an electron for conduction [18, 47]. A higher partial pressure of H_2O displaces more oxygen or donates more electrons, leading to a larger increase in current through the NW.

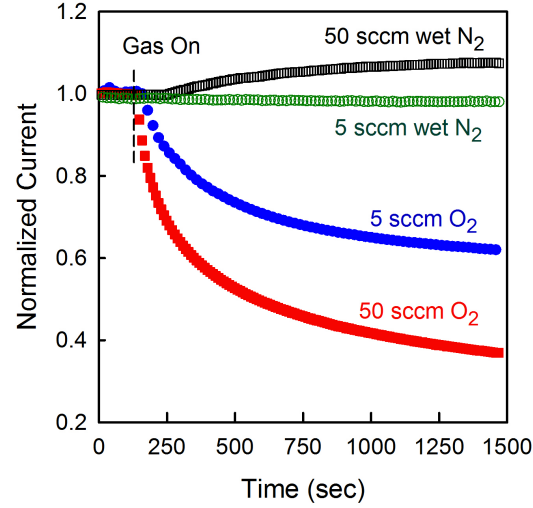


Figure 4.17: Plot of O_2 and H_2O response for different flow rates for a $5\ \mu\text{m}$ gap SRD NB device on Si/SiO_2 where $V_{DS} = 3\ \text{V}$.

Since an improvement in UV response was demonstrated when the effect of leakage through device pads was limited (see Fig. 4.6), the SiO_2/Si base substrate was replaced with a glass substrate. A $5\ \mu\text{m}$ gap SRD was subjected to 30 second UV pulses with $V_{DS} = 3\ \text{V}$; the same test performed for Fig. 4.16(b). The data presented in Fig. 4.18 is on a logarithmic scale. The uncoated data was also shown in Fig. 4.11 and is the highest I_{ON}/I_{OFF} seen in the work presented in this thesis. Over 5 orders of magnitude response was seen for an uncoated device. Albeit the parylene-A coating causes both an increase in rise and decay times as well as the previously discussed increases in photo and dark currents, it also leads to a net decrease of photosensitivity. The longer rise and decay times could be related to the parylene-A coating acting as a diffusion barrier, thereby decreasing the rate of O_2 adsorption and desorption.

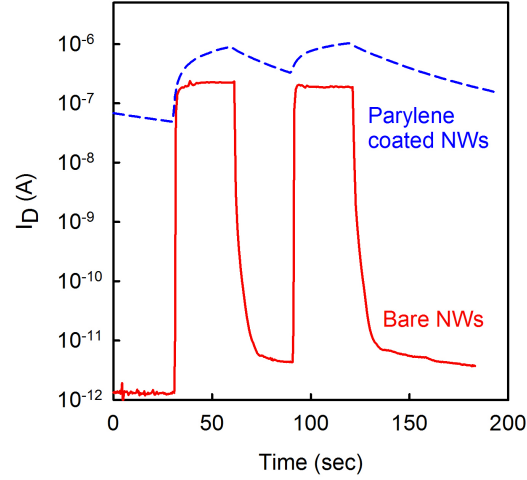


Figure 4.18: Plot of I_D over time when exposed to 30 seconds of UV with $V_{DS} = 3$ V for a $5\ \mu\text{m}$ gap SRD NB device fabricated on a glass substrate.

Fig. 4.19 shows the response of a $5\ \mu\text{m}$ gap SRD NB device to both O_2 and H_2O (wet N_2) before and after parylene-A coating. For this experiment a test gas flow rate of 50 sccm was used. As shown in this figure, both the response to O_2 and H_2O are attenuated by the parylene-A layer. For O_2 sensing it is apparent that the formation of the depletion layer, and reduction of current through the NWs, is slower after the NB has been coated in parylene-A. Also, it is possible that the parylene-A layer may also decrease the total amount of oxygen adsorbed. The time for this measurement was 800 seconds; it is possible that a longer measurement might show that the total decrease in current due to oxygen adsorption may be equivalent with or without the parylene-A layer. For these measurements, the parylene-A layer was estimated to be approximately 20 nm thick. Perhaps the increase of parylene-A layer thickness could further attenuate the signal and even-

tually completely mute contributions from O_2 and H_2O if other analytes are to be tested. One tradeoff is that the thicker the parylene-A layer becomes, the further the target analyte becomes from the transducer and the NW surface. If surface charge interactions are responsible for changing the conduction in the NW, the target analyte should be as close to the surface as possible. However, interactions with O_2 and H_2O could interfere with device sensitivity.

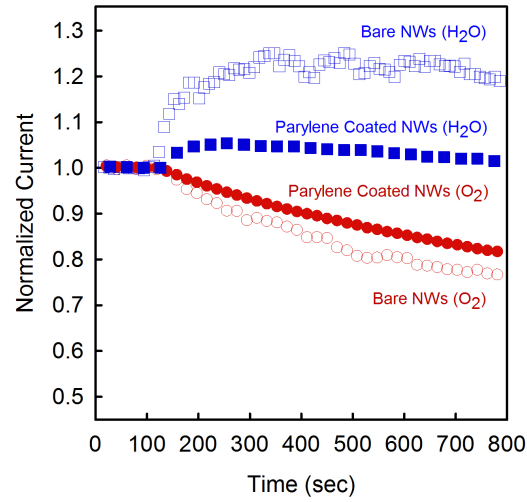


Figure 4.19: Plot of O_2 (circles) and H_2O (squares) sensing using a $5\ \mu\text{m}$ gap SRD NB device with $V_{DS} = 3\ \text{V}$ before (open) and after (closed) parylene-A coating.

4.3.3 Effect of Continuous UV Illumination on Sensor Response

In-situ illumination was implemented by incorporating a InGaN LED in the NorECs ProboStat as described in Chapter 3. ZnO NB devices were subjected to 50 sccm of test gas and the effect of UV2 illumination on device sensitivity was examined. For all measurements, $V_{DS} = 3$ V and a 2 hour N_2 purge was performed prior to measurement to achieve saturation of I_D and to obtain the normalization current.

Fig. 4.20 shows the (a) O_2 and (b) H_2O response of a ZnO NB before and after parylene-A coating, with and without UV2 illumination. As discussed in Section 4.3.2, UV illumination creates electron-hole pairs and the newly generated holes discharge surface oxygen. This process amplifies the O_2 sensing capabilities of the ZnO NB as shown by the sharp decrease in current during the earliest part of the measurement. Fig. 4.20(a) also shows that even with UV illumination, the parylene-A reduces the oxygen response. This further supports the postulate that parylene-A reduces the number of surface oxygen adsorption sites.

In the case of H_2O sensing (Fig. 4.20(b)), an initial decrease in current is observed before the NW conductivity increases if UV illumination is used during the measurement. This is possibly due to the strong relationship between UV illumination and the oxygen response. As discussed previously, the UV response of ZnO NWs is affected by both O_2 and H_2O , as determined by Li *et al.* [76]. Yoon *et al.* demonstrated that the diffusion rate for O_2 is much higher than for H_2O , this suggests that the UV response of ZnO will be dominated by O_2 [77]. This could explain the initial decrease in conductivity when H_2O sensing is performed

under UV illumination, especially if O_2 is still adsorbed on the NW surface when the measurement begins.

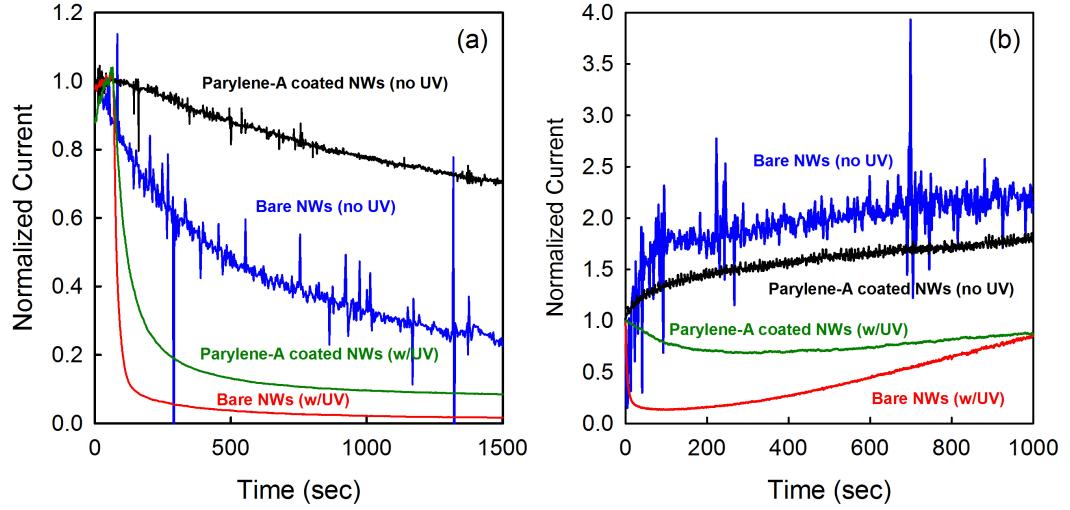


Figure 4.20: Plot of (a) O_2 and (b) H_2O sensing using a $5\ \mu m$ gap SRD NB device with $V_{DS} = 3\ V$ before and after parylene-A coating with and without in-situ UV2 illumination.

To further test the SRD NB structures, additional test gases were investigated. NW-based devices have also been used to measure a response to CO and H_2 (see Table 2.1). In these experiments, we use H_2/N_2 instead of pure H_2 . In order to use the new reducing gases the test set-up had to be moved entirely into a fumehood. To verify that the vibrations or airflow through the fumehood would not negatively impact the measurement, the same device used for the results in Fig. 20 was remeasured in the new configuration. Fig. 4.21 shows the parylene-A coated data presented in Fig. 4.20(a) and the new data taken after the measurement set-up had been moved. As shown in this figure, general device performance is consistent

and although there appears to be some additional noise with the “new O₂” data without UV illumination, the results obtained allowed the new set-up to be used for further testing.

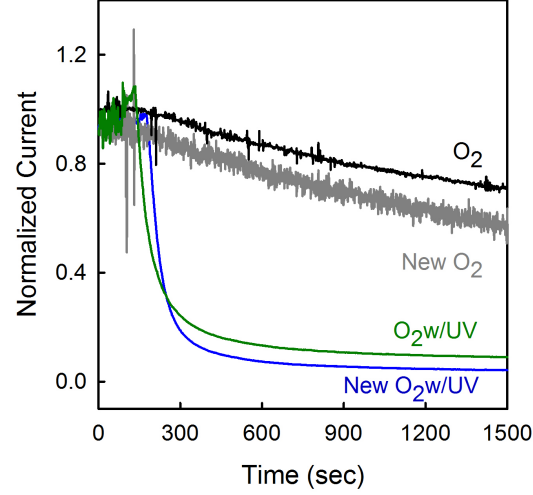


Figure 4.21: Plot of the response to a continuous O₂ flow using a 5 μm gap SRD NB device with $V_{DS} = 3\text{ V}$ after parylene-A coating with and without in-situ UV2 illumination.

To test the recovery time for the sensor, O₂ was turned on/off every 300 s. Fig. 4.22 shows the O₂ sensing and recovery of a 5 μm gap SRD NB device coated with parylene-A. The measurements were performed with and without UV2 illumination. When no UV illumination was used the signal was very noisy which can be attributed to the low device current (approximately 10 pA). At such a low current, disruptions in the ambient such as tapping or flipping the oxygen switch could be seen as a spike in the data. When UV illumination was included, the current was on the order of 10 nA so the O₂ sensing and recovery can be seen. Note that the

initial delay of the O_2 sensing response can be partially attributed to the 20 s it took for the O_2 to start flowing. The recovery time of the device was much longer than the initial O_2 sensing response. This may be because the paralyene-A acts as a diffusion layer which increases the time it takes for O_2 to return to the NW surface. Additionally, this could explain why the second O_2 sensing response is much smaller than the first. It is likely that an improvement in device recovery time would be observed for an uncoated SRD NB device.

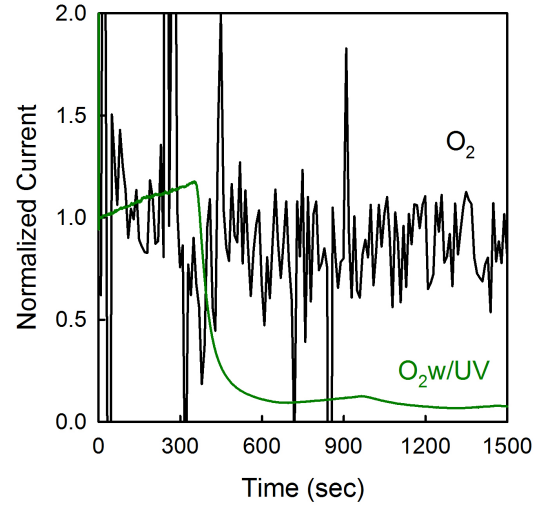


Figure 4.22: Plot of the response and recovery for a 5 μm gap SRD NB device with $V_{DS} = 3$ V after parylene-A coating when O_2 was turned on/off O_2 every 300 seconds.

The sensitivity of ZnO NBs to H_2/N_2 and CO was also investigated and the results are shown in Fig. 4.23. A flow rate of 50 sccm of test gas was used with 150 N_2 flowing throughout the entire measurement. A 5 μm gap SRD NB device coated with parylene-A was measured with $V_{DS} = 3$ V with and without UV2

illumination. Without UV illumination it was difficult to discern a reaction to either test gas because of the low device current and inherent noise. When UV illumination was used, the base NB current was increased and a response was observed. For reference, a baseline N_2 response (with UV2 illumination) is shown to depict the device drift over the time of the measurement. As expected, since CO and H_2/N_2 act as reducing gases (like H_2O), the conductivity within the NW increases when exposed. Similarly to the H_2O sensing mechanism, the conductivity increase can be explained by either the displacement of surface oxygen or the direct donation of an electron.

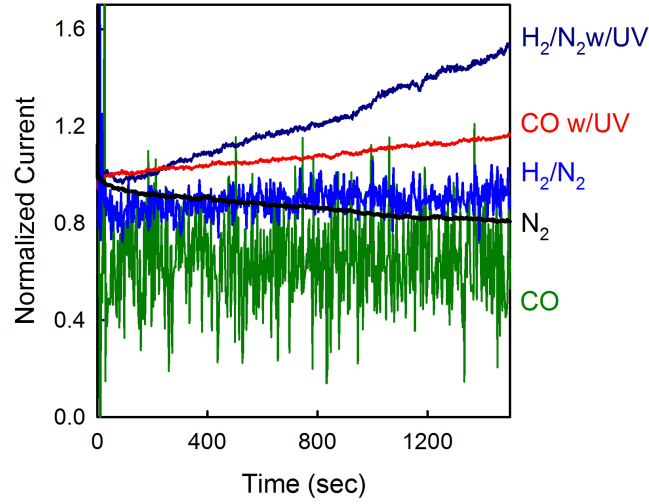


Figure 4.23: Plot of CO and H_2/N_2 sensing using a $5\ \mu\text{m}$ gap SRD NB device with $V_{DS} = 3\ \text{V}$ after parylene-A coating with and without in-situ UV2 illumination.

Chapter 5 – Summary, Conclusions and Future Work

ZnO nanbridges (NBs) were fabricated using carbonized photoresist (C-PR) as a nucleation layer. This method successfully avoids the need for a silicon-on-insulator (SOI) wafer and a metal catalyst and greatly simplifies processing. By redesigning the device to have interdigitated fingers and therefore an increased active device area, the effect of leakage through the contact pads was decreased and a greater UV response was observed. UV response was further enhanced by replacing the SiO₂/Si substrate with a better insulating glass substrate. Because ZnO NBs were found to dissolve in deionized (DI) water, a chemical vapor deposition (CVD) process was developed for parylene-A which was shown to successfully protect the NBs. The effect of the parylene-A layer on O₂, H₂O, CO, and H₂/N₂ gas sensing was investigated. In-situ UV illumination was found to improve the response time of the device to O₂ and facilitated successful sensing of CO and H₂/N₂.

Future Work

Some potential methods for further exploration utilizing the work presented in this thesis are discussed. Two possibilities for further functionalizing the ZnO NBs to achieve specific sensing are suggested.

Additional Sensing Experiments

The peak wavelength for the UV2 source used in these experiments was approximately 406 nm, corresponding to an energy of approximately 3.05 eV ($E = hc/\lambda$). The band gap of ZnO is accepted to be around 3.3 eV, with some variation in reported results. For example, Huang *et al.* report a lasing action from their ZnO nanolasers at 385 nm, corresponding to an approximate energy of 3.22 eV [78]. Although the optical spectrometer indicates that the high energy tail of the spectrum extends beyond 385 nm, using an excitation source with a lower peak wavelength could improve the UV enhancement of the gas sensing measurements. Additionally, the experiments presented in Fig. 4.22 and Fig. 4.23 were conducted only with parylene-A coated devices. Since the parylene-A acts as a diffusion layer, the recovery time for O₂ sensing and the responses to H₂/N₂ and CO could likely be improved by using an uncoated SRD NB device.

Amine Functionalization

The parylene-A layer not only acts as a protective layer for the ZnO NWs, but the amine group can be further functionalized to facilitate selective sensing. As a proof of concept, we followed experiments presented by Moon *et al.* where they showed that the amine surface density could be calculated using UV-vis techniques. In their work, an aminosilanized surface could be altered to an imine covered surface as shown in Fig. 5.1 [79]. In our work, parylene-A coated glass samples were treated using the same procedure. First, samples were immersed in anhydrous

ethanol (25 mL) containing 4-nitrobenzaldehyde (10 mg) and acetic acid (0.02 mL) in an Ar atmosphere. The solution was kept at 50 °C for 3 h. Next, the samples were washed with ethanol and sonicated in ethanol for 2 minutes prior to being dried in vacuum overnight. The following day, 10 mL H₂O and 0.02 mL acetic acid were used to hydrolyze the imines. UV-vis was used to analyze the resulting solution. For our samples the maximum absorption wavelength was between 281 and 282 nm. These values are within acceptable range of the reported literature value of 282 nm [79]. The experimentally determined average amine density was approximately 100 amines/nm² regardless of parylene-A film thickness.

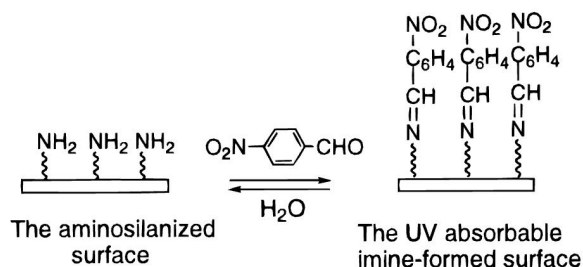


Figure 5.1: Formation of imines from the amines on an aminosilanized surface [79].

The critical conclusion from this experiment is not the exact amine density. In this work, it was proven that the amines on our parylene-A film can be altered and therefore are accessible for functionalization. One particularly interesting route for further functionalization is the attachment of an aptamer to the amine on the parylene-A. Aptamers are known for their ability to be developed for various analytes including smaller molecules [80]. Target recognition can be highly selective and the aptamer is designed for a specific analyte. Their shorter size is beneficial

for integration with this ZnO NB platform since this facilitates a smaller distance between the target analyte and the transducer [81].

SiO₂ and Silane Chemistry

An alternate to amine functionalization is exploration of the abundant options based on using SiO₂ as an activation layer [82,83]. SiO₂ was sputtered on ZnO NB devices to see if NWs could survive the sputtering process. As shown in Fig. 5.2, there is approximately 10 nm of SiO₂ on the NWs. Because of the non-conformal coating, it is very likely that the coating does not fully cover the NW, but this system could still be used as a proof of concept for developing functionalization procedures for SiO₂ on the nanoscale.

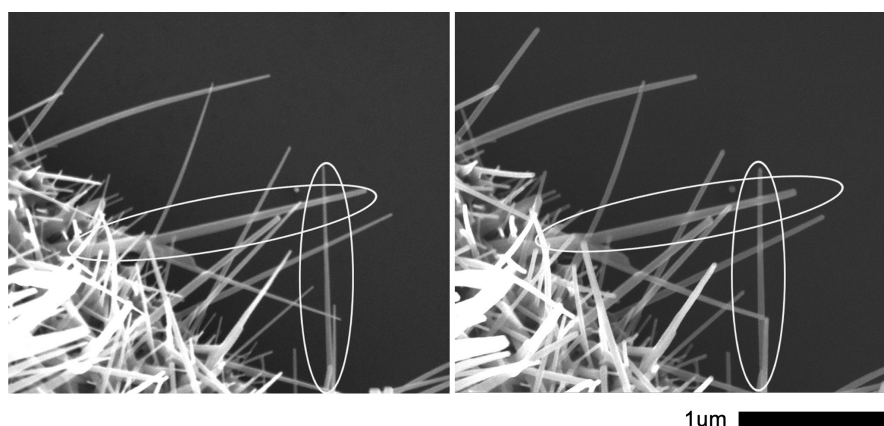


Figure 5.2: ZnO NB (a) before and (b) after sputtering SiO₂ on top of the ZnO NWs.

Selective Sensing Experiments

Very recently, Chen *et al.* demonstrated that ZnO NWs could be used to sense 2,4,6-trinitrotoluene (TNT) vapor generated from TNT powder. The authors report that they created the most sensitive TNT sensor designed using metal-oxide nanowires. Their lowest detectable concentration for TNT was approximately 60 ppb [84]. Although this sensitivity is very impressive, there were no reports about distinguishing between TNT and similar compounds. Since the sensing mechanism is attributed to the creation of NO_2 from a reaction between NO and oxygen ions on the ZnO NW surface other chemicals with an NO biproduct could cause the same response. Hence, the functionalization of ZnO NBs with aptamers using either parylene-A or SiO_2 could be a potential solution for distinguishing between TNT and a false positive.

APPENDICES

Appendix A – Microwave Growth of ZnO Nanowires

A.1 Abstract

ZnO nanowires (NWs) were grown by means of a hydrothermal method on ZnO seed layers using a research grade microwave system with integrated temperature control. The influence of growth time, temperature, precursor concentration, precursor ratio, and seed layer structure on the resulting NW morphology were studied using scanning electron microscopy (SEM). X-ray diffraction (XRD) was used to examine the crystallinity of the seed layer prior to growth. When pre-growth annealing was included as part of the surface treatment, increased crystallinity of the seed layer led to larger diameter wires. With good microwave process control, it was possible to grow uniform, vertically-oriented arrays of NWs with an angle of $1\text{--}11^\circ$ from normal and a variation in length across the sample of only $\pm 5\%$.

A.2 Introduction

Hydrothermal (solution-phase) growth methods can be used for low-temperature synthesis of ZnO nanowires (NWs), which facilitates direct growth on a variety of novel substrates otherwise prohibited by high temperature processes [36–41, 85–89, 91]. Applications requiring flexible substrates, such as energy-harvesting fabrics, could be advanced using these methods [41, 91]. Although hydrothermal

growth opens up a new realm of possible applications, one major drawback is that growth times of up to 20 hours have been reported as necessary to yield desired NW morphologies using conventional hot-plate heating [37–41]. Traditional hydrothermal growth techniques have reported growth rates between 0.2 nm/min and 10 nm/min [37, 41]. Recently, the use of a microwave oven to supply heat to the nutrient solution has been reported to accelerate the growth process by Unalan *et al.* [39], who reported ZnO growth rates as high as 100 nm/min using microwave power. Although growth temperature has been reported to be a critical process variable for hydrothermal growth [37–39], Unalan *et al.* were not able to directly control temperature with the conventional microwave oven used in their study. Instead, indirect control of growth temperature was attempted by using different fixed settings of the microwave power level.

Conventional microwave ovens change power level through variations in duty cycle, or the percentage of time that the microwave is on. In this work, a microwave system equipped with integrated temperature control was used to grow ZnO NWs by means of a hydrothermal method. The impact of growth temperature, growth time, solution concentration, and seed layer crystallinity on ZnO NW length, diameter, aspect ratio, growth orientation, density, and morphology was investigated. With optimized growth conditions and good process control, highly uniform arrays of ZnO NWs were achieved with height variation of $\pm 5\%$.

A.3 Experimental Details

ZnO nanowires were grown hydrothermally using $\text{Zn}(\text{NO}_3)_2$ and hexamethylene tetramine (HMT) as discussed in [36]. NW growths were performed in a CEM Discover S Class Microwave System which uses a 600 W magnetron to irradiate samples. Microwave irradiation is conducted in a specially designed pressure-sealed vial with controlled power, temperature, and pressure. Both temperature and pressure are monitored in-situ. Temperature was monitored by a vertically focused IR temperature sensor that was constructed within the microwave chamber, but outside the sealed vial. Pressure was monitored by a proprietary system that involves measuring the expansion of the flexible lid seal. Software continuously monitored and recorded the system pressure, temperature, growth time, and power for each experiment. For comparison, hydrothermal growth was also performed without microwave irradiation using a hot plate for 6 hours at 80 °C in a solution of 250 mL DI water, 0.19 grams $\text{Zn}(\text{NO}_3)_2$ and 0.09 grams HMT.

Hydrothermal growth took place selectively on ZnO thin film seed layers. A summary of ZnO seed layer films is presented in Table A.1. ZnO seed layer films in Groups A-D were deposited on 6" Si wafers via atomic layer deposition (ALD) using diethylzinc (DEZ) and H_2O at 170 °C. Prior to ZnO deposition, Si substrates were etched in HF to remove any native oxide film. The base thickness used for the studies was 90 nm of ZnO (Group A). Additional substrates with an underlying 10 nm buffer layer of Al_2O_3 (Group B), deposited via ALD using $\text{Al}(\text{CH}_3)_3$ and H_2O , were also used. ZnO thin films of thicknesses 15 nm, 90 nm, and 200 nm

were deposited to examine the impact of seed layer thickness (Group C). A select number of ALD films were annealed to investigate the impact of seed layer crystal structure on NW growth (Group D). Samples were either (i) rapid thermal annealed (RTA) in air for 10 minutes at 900 °C, (ii) annealed in N₂ for 10 minutes at 900 °C in a tube furnace, or (iii) annealed in N₂ for 10 minutes at 400 °C in the ALD chamber. To investigate the impact of the seed layer deposition method on NW growth, 90 nm ZnO films were also deposited via RF sputtering (Group E) at 75 W in a 15 mTorr Ar atmosphere. 7 cm x 2 cm Si coupons were placed at a working distance of 4" from the 2" ZnO target. X-ray diffraction (XRD) analysis of selected seed layers was performed using a Bruker D8 Discovery.

Table A.1: Seed layer summary

Sample Group	ZnO Thickness (nm)	Al ₂ O ₃ Buffer Thickness (nm)	Annealing Treatment	Deposition Method
A	90	-	-	ALD
B	90	10	-	ALD
C	15	-	-	ALD
	200	-	-	ALD
D	90	-	N ₂ , 900 °C	ALD
	90	-	N ₂ , 400 °C	ALD
	90	-	Air, 400 °C	ALD
	90	-	Ar, 400 °C	ALD
E	90	-	-	RF Sputtering

The first step for microwave growth was to prepare a 250 mL batch solution of $\text{Zn}(\text{NO}_3)_2/\text{HMT}$. The solution was then left stirring on a hot plate at 60 rpm at room temperature. Samples (1 cm x 1 cm) coated with a ZnO seed layer were attached to a 35 mL microwave vial using Kapton tape. When the solution was thoroughly mixed, 20 mL was measured and poured into the vial with approximately 1 cm of the solution above the sample. A magnetic stir bar was added and the vial was covered with a lid designed to control pressure. The lids, vials, and stir bars are supplied by CEM for specific use with the Discover S Class Microwave System. All samples were grown with the stirbar/agitation speed set to “low”. After growth, samples were immediately dried via wicking with KimWipes. By visual inspection, samples appeared white with varying color across the sample.

Growth times were varied from 1 minute to 12 hours. Direct control of the process temperature, which varied from 70-100 °C, was achieved using the integrated infrared temperature control. For all runs, a power limit of 50 W was used. Although this power setting appears to be lower than those used in Unalan *et al.* (120-700 W) [39], the power density in W/mL was higher for our experiments due to the small volumes (approximately 30 mL) used. At the start of the run, the Discover S Class Microwave System ramps to the set temperature with microwave power at the set limit. Once the set temperature is reached, the power drops to maintain a constant temperature.

The precursor concentrations used are presented in Table A.2. The nominal concentrations for $\text{Zn}(\text{NO}_3)_2$ and HMT were 25 mM (Group I). Solution concentration was also varied in 1:1 ratios ranging from 5 to 50 mM increments (Group II). Additionally, $\text{Zn}(\text{NO}_3)_2$ to HMT concentration ratios of 2:1 and 1:2 were used (Group III).

Table A.2: Solution concentrations summary

Sample Group	$\text{Zn}(\text{NO}_3)_2$ Concentration (mM)	HMT Concentration (mM)
I	25	25
II	50	50
	5	5
	10	10
III	5	10
	10	5
	25	50
	50	25

A Leo 1560 scanning electron microscope (SEM), operated at an accelerating voltage of 3.00 kV or 5.00 kV with a working distance of 3-8 mm, was used to assess NW morphological structure (including length, diameter, density, vertical orientation with respect to the substrate, tapering, and cross-sectional shape). Prior to imaging, a thin carbon coating was sputtered onto the sample to prevent charging and image drift. NW length, diameter, and angle with respect to the normal of the growth substrate were determined by averaging the measurements of at least five NWs within a cross-sectional image.

Error in measurements is dominated by the uniformity across the sample, which in well-controlled growths is measured to be approximately $\pm 5\%$, as discussed in the following section. All density measurements are based on the number of discernable NWs in a $1\ \mu\text{m}^2$ square of top-down SEM images. To help ensure that crystal structures on the seed layer were not being counted as NWs, an object was only counted as a NW if it appeared brighter than its surroundings.

A.4 Results and Discussion

A.4.1 Nanowire Dimensions (Length, Diameter, and Aspect Ratio)

A.4.1.1 Length vs Time

As expected, it was found that wire length increases with growth time. Shown in Fig. A.1 are plots of average length vs growth time for 1:1 concentration ratio (Group I and II shown in Table A.2) at various growth temperatures. NWs in Fig. A.1(a) were grown on 90 nm ALD ZnO seed layer films (Group A from Table A.1). NWs in Fig. 1(b) were grown on 90 nm ALD ZnO seed layer films with an underlying 10 nm thick ALD Al_2O_3 buffer layer without any buffer layer (Group B from Table A.1). The presence of the underlying buffer layer does not appear to have a large impact on NW length. NWs of roughly similar length were grown on both substrates for both $85\ ^\circ\text{C}/25\ \text{mM}$ and $70\ ^\circ\text{C}/25\ \text{mM}$ conditions.

For growth times up to 60 minutes, growth at 85 °C produced longer wires than growth at 70 °C. Growth at 100 °C/25 mM (not shown) produced wires of similar length to those grown under 85 °C/25 mM conditions. Finally, NW length did not increase with time for the 5 mM solution at 85 °C, suggesting that the low solution concentration limited growth (see A.4.1.2).

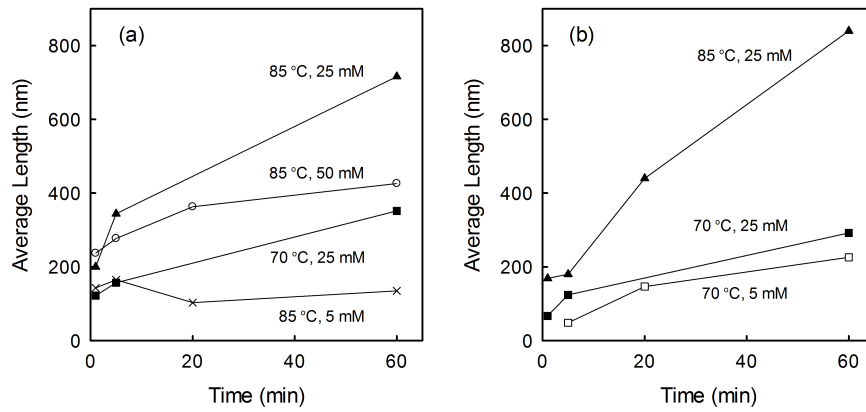


Figure A.1: Plot of average NW length vs growth time for ZnO NWs grown using various combinations of temperature and precursor concentration on either (a) 90 nm ALD ZnO films on Si or (b) 90 nm ALD ZnO films with a 10 nm thick Al₂O₃ buffer layer (ZnO/Al₂O₃/Si). Lines are to guide the eye.

Shown in Fig. A.2 are a series of representative top-down and cross-sectional SEM images that illustrate NW growth as a function of time. All NWs were grown on ZnO/Al₂O₃/Si substrates (Group B from Table A.1), using a 25 mM (1:1) solution at 85 °C (Group I from Table A.2). The top-down image in Fig. A.2(b) makes it appear that the diameter of the wires is changing, but the NWs in this sample are tapered (as shown in cross-sections of Fig. A.2(b) and (c)) as a result of a process control issue described in section A.4.6).

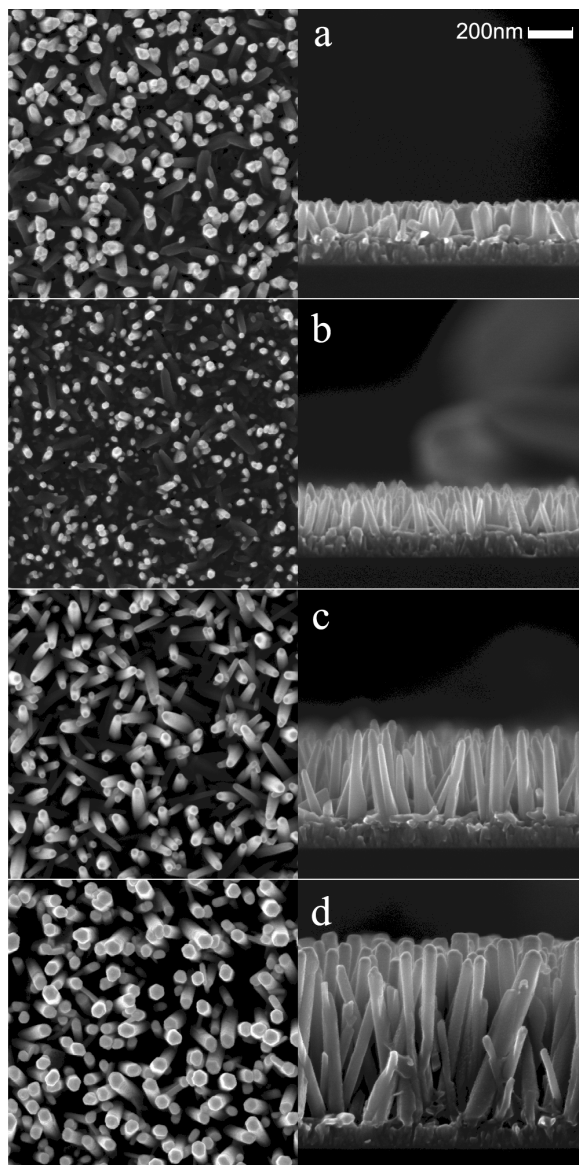


Figure A.2: SEM images illustrating NW growth on ZnO/Al₂O₃/Si substrates using a 25 mM (1:1) solution at 85 °C after (a) 1 min, (b) 5 min, (c) 20 min, and (d) 60 min of growth time.

A.4.1.2 Length vs Concentration

Shown in Fig. A.3 is a plot of average NW length vs concentration for 1:1 $\text{Zn}(\text{NO}_3)_2$ to HMT precursor ratios (Group I and II in Table A.2) and temperatures of 70 °C and 85 °C on either (a) ZnO films on Si (Group A from Table A.1) or (b) 90 nm ALD ZnO films with 10 nm thick Al_2O_3 buffer layers (Group B from Table A.1) as a seed layer. For both ZnO/Si and ZnO/ Al_2O_3 /Si seed layers with 1:1 solution concentration, the average NW length was seen to increase until 25 mM was reached. The average length of both the 70 °C and 85 °C growths conducted at 50 mM were actually shorter than the average length at 25 mM, suggesting

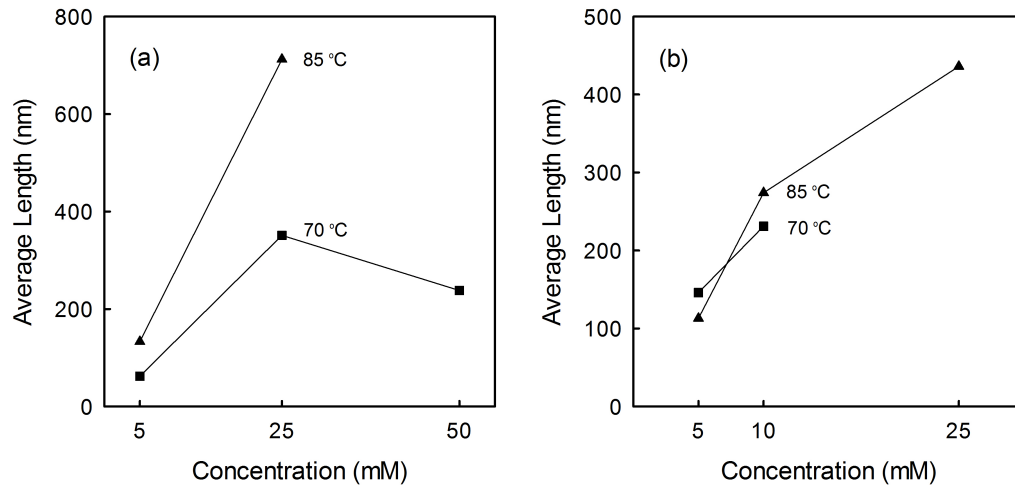


Figure A.3: Plot of NW length vs 1:1 precursor concentration for NWs that were grown for either (a) 60 minutes on 90 nm ALD ZnO films on Si or (b) 20 minutes on 90 nm ALD ZnO films with a 10 nm thick Al_2O_3 buffer layer (ZnO/ Al_2O_3 /Si). Lines are to guide the eye.

that excess HMT limits the reaction, as suggested by Xu *et al.* [38]. For 5 mM concentration, the growth rate was small, suggesting that the low concentration is limiting the deposition rate. This is also seen in Fig. A.1(b), where an 85 °C, 5 mM growth shows only a small change in length over time. Furthermore, it is possible that with this growth method, there is a competition between the reaction creating the wires and aquatic etching of the NWs, since ZnO is known to dissolve in water [24].

The impact of the ratio between the $\text{Zn}(\text{NO}_3)_2$ and HMT concentrations was also investigated. Fig. A.4 shows the dependence of NW length on concentration ratios. There is not only a dependence on the concentration ratio, but the amount of the precursor used; this is clearly apparent when the concentration ratio is 1:2.

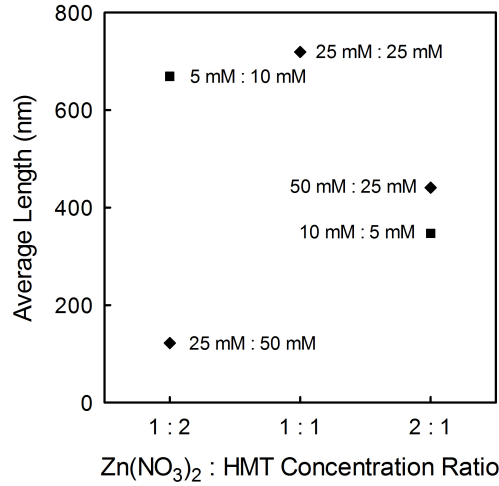


Figure A.4: Plot of NW length vs concentration ratio for various precursor concentrations on 90 nm ZnO on Si.

The HMT is expected to make the solution more basic and assist in the formation of the ZnO NWs, but as mentioned Mason *et al.* [88], it is likely that only a minimum amount of HMT is needed for the growth process. In these experiments, all growths produced NWs, so the minimum amount of HMT needed has not yet been determined.

A.4.1.3 Longest Wires

The maximum obtainable length appears to be a limitation of the microwave hydrothermal growth method. For a growth time of 60 minutes, the longest NWs achieved on a 90 nm ZnO seed layer were 716 nm long, using a 25 mM solution (1:1 concentration ratio) at 85 °C. For a thicker 200 nm ZnO seed layer, NWs up to 1 μm in length were obtained using the same growth conditions. Using the same growth conditions on a 90 nm ZnO/Al₂O₃/Si substrate, the maximum length obtained in 60 minutes was 821 nm. Even for an overnight (12 hour) growth, the maximum length achieved was less than 1 μm . The saturation of NW length for long growth times is likely due to the complete consumption of available precursors [90]. Refreshing the solution or using chemical additives such as polyethylene imine (PEI) may possibly increase the NW length [24, 86, 92]. Using a continuous flow system as demonstrated by Morin *et al.*, longer wires could be grown using similar precursor concentrations [90]. Alternatively, there are applications for short nanowires such as growth on Kevlar for energy harvesting applications [91].

A.4.1.4 Diameter

For a given substrate, diameter only slightly depends on growth time, temperature, or concentration. For all growths on 90 nm ALD ZnO seed layers, the average NW diameter was $70(\pm 6)$ nm. However, as discussed below, the morphological structure of the seed layer was found to have a strong impact on the NW diameter.

A.4.1.5 Aspect Ratio

Shown in Fig. A.5 is a plot of average aspect ratio for NWs grown under various conditions on a ZnO/Al₂O₃/Si substrate. Within a single set of run conditions, it was seen that the aspect ratio tends to increase with time. Since NWs were typically the same diameter for all growth conditions (excluding seed layer dependence), process parameters that produced longer wires also typically had higher aspect ratios. In all samples with a 1 hour or less growth time the maximum aspect ratio obtained was approximately 13. This aspect ratio was obtained using a 90 nm ALD ZnO seed layer with a 10 nm buffer layer, 85 °C growth temperature, 60 minute growth time, and a concentration ratio of 1:1 with a 25 mM concentration.

The diameter of NWs grown on ZnO seed layers with an Al_2O_3 buffer layer was 45 ± 17 nm, which was thinner than NWs grown on ZnO seed layer films deposited directly on Si, (typically 70 nm). However, since the wires which were grown on substrates with the Al_2O_3 buffer layer were also typically shorter (excluding Group I at 85 °C for 60 minutes) than those without the buffer layer, the aspect ratio is not significantly different.

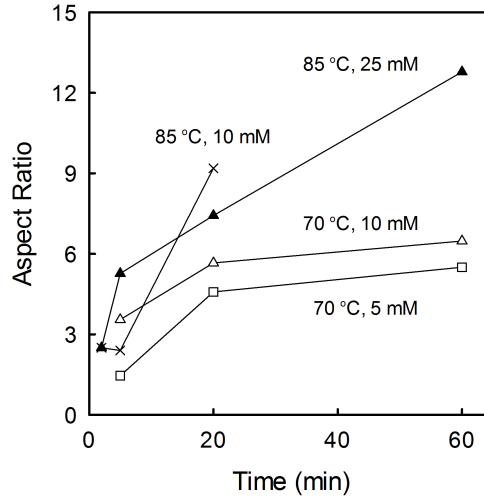


Figure A.5: Aspect ratio as a function of growth time for NWs grown on ALD ZnO films with a 10 nm thick Al_2O_3 buffer layer ($\text{ZnO}/\text{Al}_2\text{O}_3/\text{Si}$) at various temperatures and concentrations. Lines are to guide the eye.

A.4.2 Density

NW density (number of NWs/ μm^2) does not appear to be strongly dependent on precursor concentration, time, or temperature. Typical top-down SEM images in-

dicating NW density are shown in Fig. A.2. An average density of $180 \text{ NWs}/\mu\text{m}^2 \pm 90 \text{ NWs}/\mu\text{m}^2$ was observed for all runs on 90 nm ALD ZnO seed layers, with or without buffer layers. There was not a distinct change in density with the addition of an Al_2O_3 buffer layer. Note that since all analyses were performed manually from analysis of top-down SEM images, NW density results are only an approximation.

A.4.3 Orientation

For all growths performed, NWs were found to be oriented roughly perpendicular to the surface with an average angle from normal of $6^\circ \pm 5^\circ$. NW orientation was not found to be strongly dependent upon precursor concentration, growth temperature, or time.

A.4.4 Impact of Seed Layer and Substrate

Fig. A.6 shows top-down and cross-sectional images for NW growth on the seed layers from Groups C, D and E (in Table A.1). All results are from Group I (see Table A.2), and were grown at a temperature of 85°C for 60 minutes. Fig A.6(a) and (b) show the morphological differences (tapering, density, diameter) that result from an increase in ALD ZnO seed layer thickness from 15 nm to 200 nm. NWs grown on 90 nm ZnO had a larger diameter when the seed layer was annealed at 900°C prior to growth in either (c) N_2 or (e) air than when it was annealed at only (d) 400°C in N_2 . For example, for N_2 annealed samples, NWs produced were

almost 400 nm in diameter and over a 1000 nm tall. As for the effect of anneal ambient, NWs annealed in air (e) were found to be more tapered than those where the substrate was annealed in N_2 (c). The 90 nm thick sputtered films seeded NWs similar to those in (a), but with improved orientation towards the substrate normal.

Others have reported that the growth substrate can have a large influence on NW morphology. Song *et al.* and Breedon *et al.* showed that the seed layer has a strong impact on NW morphological structure and that the orientation of the seed layer can affect the growth rate and the diameter of the ZnO nanowires [93, 94]. In addition, vertically-aligned arrays grown by J.H. Lee *et al.* showed a high dependence on the seed layer and substrate [95]. The prepared substrates were Si with ZnO nanoparticles and a ZnO seed layer on ZnO foil. Their results showed that for low concentrations and temperatures the ZnO NWs could not be seeded on the pre-cast Si, but the ZnO seed layer on the ZnO foil would still seed growth and that the alignment and diameter of the NWs would be more uniform [95]. Also, as demonstrated by Conley *et al.* [32], different methods of depositing the same seed material can be used to alter NW morphological structure. In their study, ZnO ALD films and metal-organic spinon deposition (MOD) were both used to seed ZnO NWs. Additionally, in this work, thicker NWs are seen on doped ZnO seed layers (both p- and n-type), that are annealed after ion implantation. Depending on the process of the ZnO seed creation, the constituents present, and any pre-growth anneals the morphological structure of the NWs change.

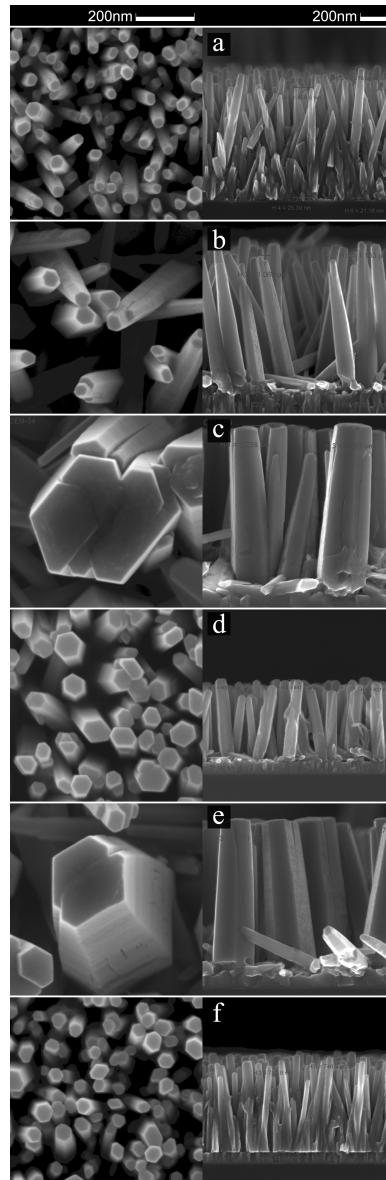


Figure A.6: SEM images of Group I (see Table A.1) growth on (a) 15 nm thick ALD ZnO films, (b) 200 nm thick ALD ZnO films, (c) 90 nm ALD ZnO films annealed in N_2 at 900 °C, (d) 90 nm ALD ZnO films annealed in N_2 at 400 °C, (e) 90 nm ALD ZnO films annealed in air at 900 °C, and (f) 90 nm sputtered ZnO films.

XRD was performed on seed layers from Groups A, B, D and E. The scans were performed from 30° to 37° in 2θ with a step size of 0.01° to examine the highest intensity peaks in ZnO. Fig. A.7 shows the data vertically offset, for visualization. There appears to be little structural difference between the 90 nm ZnO seed layer (Fig. A.7(a)) and the seed layer which has a 10 nm buffer layer of Al_2O_3 (Fig. A.7(b)). When a high temperature anneal (900°C in either N_2 or air) is included as part of the seed treatment prior to NW growth (Fig. A.7(c) and (d)), the film crystallinity increases as expected. As seen in SEM images Fig. A.6(c) and (e), these more crystalline films result in growth of NWs with a larger diameter (similarly to work by Liu *et al.* [96]). Also found in XRD scans, a secondary phase is formed during a high temperature anneal (in both N_2 and atmosphere). Given the constituents present and the location of the peak, it is possible that the second phase is Zn_2SiO_4 [97]. The relative intensities of the ZnO c-axis peak and the secondary phase peak (Fig. A.7(d)) also indicate that an oxidizing environment promotes the formation of this second phase at the expense of crystalline ZnO, the contrary is true in N_2 (Fig. A.7(d)). This observation is in agreement with the second phase being an oxide of Zn and Si (i.e., Zn_2SiO_4). The increased diameter of the NWs grown on annealed layers is likely due to the increase in the grain size at high annealing temperatures, which seeds NW growth.

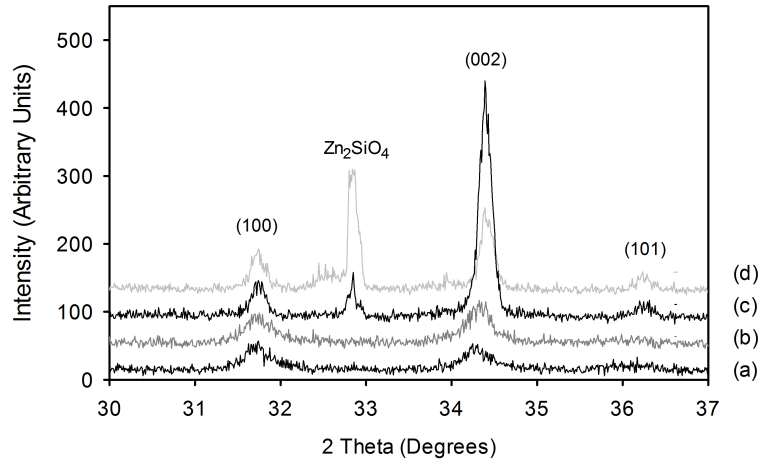


Figure A.7: XRD data showing crystalline peaks for (a) 90 nm ALD ZnO as deposited, (b) 10 nm ALD Al₂O₃ buffer and 90 nm ZnO seed layer as deposited, (c) 90 nm ALD ZnO annealed in N₂ at 900 °C and (d) 90 nm ALD ZnO annealed in O₂ at 900 °C. Data is vertically offset for visualization.

A.4.5 Crystallites

One of the challenges encountered with hydrothermal growth using a hot plate is the undesirable homogeneous nucleation resulting in the growth of crystallites in the bulk of the solution and subsequent deposition on the growth substrate [88,98]. In agreement, Qurashi *et al.* saw similar crystallites when their samples did not have a seed layer [99]. Fig. A.8 shows SEM images comparing hydrothermal growth using either (a) a hot plate and (b) the microwave as the heating mechanism. When the solution of 250 mL DI water, 0.19 grams Zn(NO₃)₂ and 0.09 grams HMT was heated for 6 hours at 80 °C, crystallites (indicated in (a)) were 2-4 μm long and approximately 300 nm wide. These crystallites appeared in nearly every

run performed using a hot plate; however, no large crystallites were found in any of the microwave runs that exhibited good process control. A possible explanation for this is an increase in local solution temperature compared to the bulk solution. As described by Collins [100], unlike thermal conduction used in conventional heating, microwaves can penetrate the sample container and superheat local areas within the solution. Because of this localized heating, the reaction in a specific area may consume the available precursors for NW formation, and supersede the formation of larger crystals.

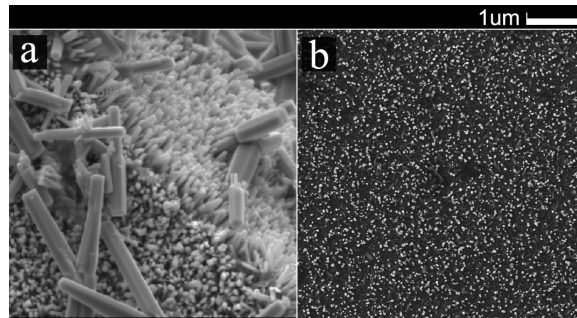


Figure A.8: Hot plate growths had additional crystallites which covered the surface of the sample as shown in (a). Well-controlled microwave growths were free of unwanted crystallites as shown in (b).

A.4.6 Process Control

As shown in Fig. A.9(a), with good process control, NW length variation across a 1 cm x 1 cm sample was as low as only 5%. The resulting morphology and quality of the arrays grown was found to depend on the performance of the pressure control lid. When the lid performs well, pressure is maintained and the process is

well controlled. The system ramps to maximum set temperature in a fairly constant amount of time and achieves maximum set temperature without overshoot. After reaching maximum temperature, the temperature is held steady throughout the run with little power input. With good process control, good NW length uniformity is achieved and NW length is a well-behaved function of time, precursor concentration, temperature, and seed layer structure.

On the other hand, if the lid used in the experiment does not seal completely, pressure in the vial is not maintained. The lack of pressure control allows evaporation from the vial and cooling, resulting in an increase in the amount of time it takes to ramp to maximum temperature, overshoot of maximum temperature, and fluctuation of power and temperature after maximum temperature is reached. These runs result in shorter NWs (approximately 240nm) with poor across-sample uniformity across the sample ($\pm 30\%$), and loss of a strong hexagonal structure (shown in Fig A.9(b)). When the lid was mostly sealed, an intermediate or medium controlled run seeded NWs that were 740 nm long $\pm 17\%$ across the sample.

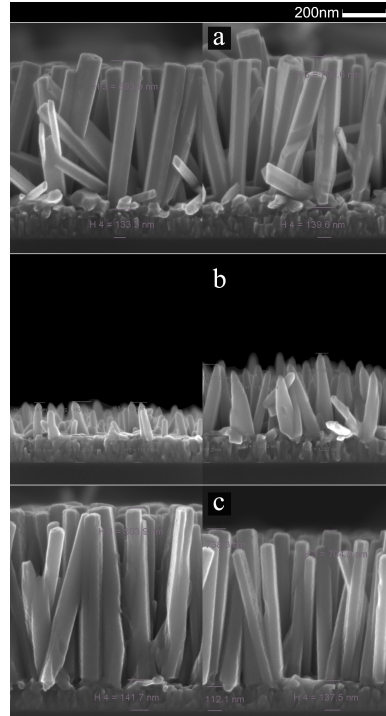


Figure A.9: Process control effects on growth morphology depicting: (a) well-controlled growth with consistent NW lengths and uniformity across the sample, (b) poorly controlled growth with altered morphology and wide variation in length and (c) a moderately well-controlled growth.

A.5 Summary and Conclusions

ZnO NWs were grown via a hydrothermal method using a research grade microwave with an integrated IR temperature controller. Specialized lids, vials and stirbars were used for the experiments. The influence of growth temperature, growth time, solution concentration, and seed layer crystallinity on ZnO NW length, diameter, aspect ratio, growth orientation, density, and morphology was investigated. Resulting NW morphology was found to be dominated by the effects of the seed

layer. For example, annealing at 900 °C in either air or N₂ increased the seed layer crystallinity, which in turn increased NW diameter, demonstrating quasi-epitaxial growth of the NWs. NWs longer than 1 μ m could be grown by integrating a continuous flow system, similar to work by Morin *et al.* [90], into the microwave system. It was found that the microwave was capable of achieving very uniform growth. With good process control, vertically-oriented NWs with low taper and lengths of 716 nm with only $\pm 5\%$ variation across the sample were obtained for 25 mM, 1:1 ratio of precursors, at a growth temperature of 85 °C and growth time of 60 minutes. These NWs are similar in length to those used by Choi *et al.* [101] for their piezoelectric-inspired device. The uniformity across the sample will help ensure a larger number of contacts to the NWs and more consistent bending in each NW. Additionally, larger crystallites are not formed using this method, so the quality of the arrays will not be degraded.

Bibliography

- [1] G.H. Li, T. Gao, Y.G. Wang, and T.H. Wang, “Adsorption and Desorption of Oxygen Probed from ZnO Nanowire Films by Photocurrent Measurements,” *Appl Phys Lett* vol. 86, p. 123117 (3 pp), 2005.
- [2] P. Offermans, M. Crego-Calama, and S.H. Brongersma, “Gas Detection with Vertical InAs Nanowire Arrays,” *Nano Letters*, vol. 10, pp. 2412-2415, May 2010.
- [3] Y. Cui, Q. Wei, H. Park, and C. M. Lieber, “Nanowire Nanosensors for Highly Sensitive and Selective Detection of Biological and Chemical Species,” *Science*, vol. 293, pp. 1289-1292, Aug. 2001.
- [4] Y.-J. Choi, I.-S. Hwang, J.-G. Park, K.J. Choi, J.-H. Park, and J.-H. Lee, “Novel Fabrication of an SnO₂ Nanowire Gas Sensor with High Sensitivity,” *Nanotechnology* vol. 19, p. 095508 (4 pp), Feb. 2008.
- [5] J.B.K. Law and J.T.L. Thong, “Improving the NH₃ Gas Sensitivity of ZnO Nanowire Sensors by Reducing the Carrier Concentration,” *Nanotechnology*, vol. 19, pp. 205502 (5 pp), Apr. 2008.

- [6] Y. Xia, P. Yang, Y. Sun, Y. Wu, B. Mayers, B. Gates, Y. Yin, F. Kim, and H. Yan, "One-Dimensional Nanostructures: Synthesis, Characterization, and Applications," *Adv Mater*, vol. 15, pp. 353-389, Mar. 2003.
- [7] Z.L. Wang, "Zinc Oxide Nanostructures: Growth, Properties and Applications," *Journal of Physics: Condensed Matter* vol. 16, R829-R858, Jun. 2004.
- [8] M. Law, J. Goldberg, and P. Yang, "Semiconductor Nanowires and Nanotubes," *Annu Rec Mater Res*, col. 34, pp. 83-112, Aug. 2004.
- [9] E. Comini, "Metal Oxide Nano-Crystals for Gas Sensing," *Anal Chim Acta*, vol. 568, pp. 28-40, 2006.
- [10] N.S. Ramgir, Y. Yang, and M. Zacharias, "Nanowire-Based Sensors," *Small*, vol. 6, pp. 1705-1722, 2010.
- [11] M.-W. Ahn, K.S. Park, J.-H. Heo, D.-W. Kim, K.J. Choi, and J.-G. Park, "On-chip Fabrication of ZnO-Nanowire Gas Sensor with High Gas Sensitivity," *Sensor Actuat B-Chem*, vol. 138, pp. 168-173, Apr. 2009.
- [12] J.S. Wright, W. Lim, D.P. Norton, S.J. Pearton, F. Ren, J.L. Johnson, and A. Ural, "Nitride and Oxide Semiconductor Nanostructured Hydrogen Gas Sensors," *Semicond Sci Technol*, vol. 25, p. 024002 (8 pp), Jan. 2010.
- [13] Q. Wan, Q.H. Li, J. Chen, T.H. Wang, X.L. He, L.P. Li, and C.L. Lin, "Fabrication and Ethanol Sensing Characteristics of ZnO Nanowire Gas Sensors," *Appl Phys Lett*, vol. 84, pp. 3654-3656, May 2004.

- [14] Y. Zeng, T. Zhang, M. Yuan, M. Kang, G. Lu, R. Wang, H. Fan, Y. He, and H. Yang, "Growth and Selective Acetone Detection Based on ZnO Nanorod Arrays," *Sensor Actuat B-Chem*, vol. 143, pp. 93-98, Dec. 2009.
- [15] J.G. Lu, P. Chang, and Z. Fan, "Quasi-One-Dimensional Metal Oxide Materials – Synthesis, Properties and Applications," *Mat Sci Eng R*, vol. 52, pp. 49-91, 2006.
- [16] C. Cheng, M. Lei, L. Feng, T.L. Wong, K.M. Ho, K.K. Fung, M.M.T Loy, D. Yu, and N. Wang, "High-Quality ZnO Nanowire Arrays Directly Fabricated from Photoresists," *ACS Nano*, vol. 3, pp. 53-58, 2009.
- [17] B. Pelatt, C.-C. Huang, and J.F. Conley Jr., "ZnO Nanobridge Devices Fabricated using Carbonized Photoresist," *Solid State Electron*, vol. 54, pp. 1143-1149, 2010.
- [18] C.-C. Huang, B. Pelatt, and J.F. Conley Jr., "Directed Integration of ZnO Nanobridge Sensors using Photolithographically Patterned Carbonized Photoresist," *Nanotechnology*, vol. 21 p. 195307, 2010.
- [19] E.A. Bayer and M. Wilchek, "The Use of the Avidin-Biotin Complex as a Tool in Molecular Biology," *Methods Biochem Anal*, vol. 26, pp. 1-45, 1980.
- [20] N.M. Green, "Avidin and Streptavidin," *Methods Enzymol*, vol. 184, pp. 51-67, 1990.

- [21] M. Wilchek, E.A. Bayer, and O. Livnah, "Essentials of Biorecognition: The (Strept)avidin-Biotin System as a Model for Protein-Protein and Protein-Ligand Interaction," *Immunol Lett*, vol. 103, pp. 27-32, Feb. 2006.
- [22] D.J. Hnatowich, F. Virzi, and M. Rusckowski, "Investigations of Avidin and Biotin for Imaging Applications," *J Nucl Med* vol. 28, pp. 1294-1302, 1987.
- [23] A.D. Mason, C.-C. Huang, S. Kondo, M.T. Koesdjojo, Y.H. Tennico, V.T. Remcho, and J.F. Conley, Jr., "Synthesis, Functionalization, and Environmental Stabilization of ZnO Nanobridge Transducers for Gas and Liquid-Phase Sensing," *Sensor Actuat B-Chem*, vol. 155, pp. 245-252, 2011.
- [24] J. Zhou, N. Xu, and Z.L. Wang, "Dissolving Behavior and Stability of ZnO Wires in Biofluids: A Study on Biodegradability and Biocompatibility of ZnO Nanostructures," *Adv Mater*, vol. 18, pp. 2432-2435, 2006.
- [25] J. Miwa, Y. Suzuki, and N. Kasagi, "Adhesion-based Cell Sorter with Antibody-immobilized Functionalized-parylene Surface," *MEMS 2007, Kobe, Japan*, pp. 27-30, 2007.
- [26] B.-J. Jeon, M.-H. Kim, and J.-C. Pyun, "Application of a Functionalized Parylene Film as a Linker Layer of SPR Biosensor," *Sensor Actuat B-Chem*, vol. 154, pp. 89-95, Jun. 2011.
- [27] S.L. Clark and V.T. Remcho, "Electrochromatographic Retention Studies on a Flavin-binding RNA Aptamer Sorbent," *Anal Chem*, vol. 75, pp. 5692-5696, Sep. 2003.

- [28] R.S. Wagner and W.C. Ellis, “Vapor-Liquid-Solid Mechanism of Single Crystal Growth,” *Appl Phys Lett*, vol. 4, pp. 89-90, Mar. 1964.
- [29] R.S. Wagner, W.C. Ellis, K.A. Jackson, and S.M. Arnold, “Study of the Filamentary Growth of Silicon Crystals from the Vapor,” *J Appl Phys*, vol. 35, pp. 2993-3000, Oct. 1964.
- [30] G. Cao, *Nanostructures and Nanomaterials: Synthesis, Properties and Applications*, London: Imperial College Press, 2006.
- [31] M.H. Huang, Y. Wu, H. Feick, N. Tran, E. Weber, and P. Yang, “Catalytic Growth of Zinc Oxide Nanowires by Vapor Transport,” *Adv Mater*, vol. 13, pp. 113-116, Jan. 2001.
- [32] J.F. Conley, Jr., L. Stecker, and Y. Ono, “Directed Assembly of ZnO Nanowires on a Si Substrate without a Metal Catalyst using a Patterned ZnO Seed Layer,” *Nanotechnology*, vol. 16, pp. 292-296, Jan. 2005.
- [33] B.D. Yao, Y.F. Chan, and N. Wang, “Formation of ZnO Nanostructures by a Simple Way of Thermal Evaporation,” *Appl Phys Lett* vol. 81, pp. 757-759, Jul. 2002.
- [34] H. Lv, D.D. Sang, H.D. Li, X.B. Du, D.M. Li, and G.T. Zou, “Thermal Evaporation Synthesis and Properties of ZnO Nano/Microstructures Using Carbon Group Elements as Reducing Agents,” *Nanoscale Res Lett* vol. 5, pp. 620-625, Jan. 2010.

- [35] J.F. Conley, Jr., L. Stecker, and Y. Ono, “Directed Integration of ZnO Nanobridge Devices on a Si Substrate,” *Appl Phys Lett*, vol. 87, p. 223114 (3 pp), Nov. 2005.
- [36] L. Vayssieres, “Growth of Arrayed Nanorods and Nanowires of ZnO from Aqueous Solutions,” *Adv Mater*, vol. 15, pp. 464-466, Mar. 2003.
- [37] Q. Li, V. Kumar, Y. Li, H. Zhang, T.J. Marks, and R.P.H. Chang, “Fabrication of ZnO Nanorods and Nanotubes in Aqueous Solutions,” *Chem Mater*, vol. 17, pp. 1001-1006, Feb. 2005.
- [38] S. Xu, C. Lao, B. Weintraub, and Z.L. Wang, “Density-controlled growth of aligned ZnO nanowire arrays by seedless chemical approach on smooth surfaces,” *J Mater Res*, vol. 23, pp. 2072-2077, Aug. 2008.
- [39] H.E. Unalan, P. Hiralal, N. Rupesinghe, S. Dalal, W.I. Milne, and G.A.J. Amaratunga, “Rapid Synthesis of Aligned Zinc Oxide Nanowires,” *Nanotechnology* vol. 19, p. 255608 (5 pp), May 2008.
- [40] Y. Tong, Y. Liu, L. Dong, D. Zhao, J. Zhang, Y. Lu, D. Shen, and X. Fan, “Growth of ZnO Nanostructures with Different Morphologies by Using Hydrothermal Techniques,” *J Phys Chem B*, vol. 110, pp. 20263-20267, Sep. 2006.
- [41] S. Baruah, C. Thanachayanont, and J. Dutta, “Growth of ZnO Nanowires on Nonwoven Polyethylene Fibers,” *Science and Technology of Advanced Materials*, vol. 9, pp. 1-8, Jun. 2008.

- [42] E.M. Freer, O. Grachev, X. Duan, S. Martin, and D.P. Stumbo, “High-Yield Self-Limiting Single-Nanowire Assembly with Dielectrophoresis,” *Nature Nanotech*, vol. 5, pp. 525-530, Jul. 2010.
- [43] V.-V. Ng, *Integration of Vapor-Solid Grown ZnO Nanowires Through Dielectrophoresis*, Oregon State University Master’s Thesis, 2010.
- [44] S.H. Lee, H.J. Lee, K. Ino, H. Shiku, T. Yao, and T. Matsue, “Microfluid-Assisted Dielectrophoretic Alignment and Device Characterization of Single ZnO Wires,” *J Phys Chem C*, vol. 113, pp. 19376-19381, 2009.
- [45] M.S. Islam, S. Sharma, T.U. Kamins, and R.S. Williams, “A Novel Interconnection Technique for Manufacturing Nanowire Devices,” *Appl Phys A* vol. 80, pp. 1133-1140, Mar. 2005.
- [46] A. Chaudhry, V. Ramamurthi, E. Fong, and M.S. Islam, “Ultra-Low Contact Resistance of Epitaxially Interfaced Bridged Silicon Nanowires,” *Nano Letters* vol. 7, pp. 1536-1541, May 2007.
- [47] D.-S. Kang, S.K. Han, J.-H. Kim, S.M. Yang, J.G. Kim, S.-K. Hong, D. Kim, H. Kim, “ZnO Nanowires Prepared by Hydrothermal Growth Followed by Chemical Vapor Deposition for Gas Sensors,” *J Vac Sci Technol B*, vol. 27, pp. 1667-1672, Jun. 2009.
- [48] Q.H. Li, Y.X. Liang, Q. Wan, and T.H. Wang, “Oxygen Sensing Characteristics of Individual ZnO Nanowire Transistors,” *Appl Phys Lett*, vol. 85, pp. 6389-6391, Dec. 2004.

- [49] Z. Liu, T. Yamazaki, Y. Shen, T. Kikuta, N. Nakatani, and Y. Li, "O₂ and CO Sensing and Ga₂O₃ Multiple Nanowire Gas Sensors," *Sensor Actuat B-Chem*, vol. 129, pp. 666-670, 2008.
- [50] A. Vomiero, S. Bianchi, E. Comini, G. Faglia, M. Ferroni, and G. Sberveglieri, "Controlled Growth and Sensing Properties of In₂O₃ Nanowires," *Cryst Growth Des*, vol. 6, pp. 2500-2504, 2007.
- [51] C.S. Rout, K. Ganesh, A. Govindaraj, and C.N.R. Rao, "Sensors for the Nitrogen Oxides, NO₂, NO and N₂O, based on In₂O₃ and WO₃ Nanowires," *Appl Phys A*, vol. 85, pp. 241-246, 2006.
- [52] D. Zhang, Z. Liu, C. Li, T. Tang, X. Liu, S. Han, B. Lei, and C. Zhou, "Detection of NO₂ down to ppb Levels Using Individual and Multiple In₂O₃ Nanowire Devices," *Nano Letters*, vol. 4, pp. 1919-1924, 2004.
- [53] D. Zhang, C. Li, X. Liu, S. Han, T. Tang, and C. Zhou, "Doping Dependent NH₃ Sensing of Indium Oxide Nanowires," *Appl Phys Lett*, vol. 83, pp. 1845-1847, Sep. 2003.
- [54] C. Xiangfeng, W. Caihong, J. Dongli, and Z. Chenmou, "Ethanol Sensor Based on Indium Oxide Nanowires Prepared by Carbothermal Reduction Reaction," *Chem Phys Lett*, vol. 399, pp. 461-464, 2004.
- [55] J.X. Wang, X.W. Sun, Y. Yang, H. Huang, Y.C. Lee, O.K. Tan, and L. Vayssieres, "Hydrothermally Grown Oriented ZnO Nanorod Arrays for Gas Sensing Applications," *Nanotechnology*, vol. 17, pp. 4995-4998, 2006.

- [56] T.-J. Hsueh, C.-L. Hsu, S.-J. Chang, and I.-C. Chen, “Laterally Grown ZnO Nanowire Ethanol Gas Sensors,” *Sensor Actuat B-Chem*, vol. 126, pp. 463-477, 2007.
- [57] F.-H. Ramirez, S. Barth, A. Tarancon, O. Casals, E. Pellicer, J. Rodriguez, A.R. Rodriguez, J.R. Morante, and S. Mathur, “Water Vapor Detection with Individual Tin Oxide Nanowires,” *Nanotechnology*, vol. 18, p. 424016 (6 pp), 2007.
- [58] B. Wang, L.F. Zhu, Y.H. Yang, N.S. Xu, and G.W. Yang, “Fabrication of a SnO₂ Nanowire Gas Sensor and Sensor Performance for Hydrogen,” *J Phys Chem C*, vol. 112, pp. 6643-6647, 2008.
- [59] A. Kolmakov, Y. Zhang, G. Cheng, and M. Moskovits, “Detection of CO and O₂ using Tin Oxide Nanowire Sensors,” *Adv Mater*, vol. 15, pp. 997-1000, 2003.
- [60] L. Qin, J. Xu, X. Dong, Q. Pan, Z. Cheng, Q. Xiang, and F. Li, “The Template-Free Synthesis of Square-Shaped SnO₂ Nanowires: The Temperature Effect and Acetone Gas Sensors,” *Nanotechnology*, vol. 19, p. 185705 (8 pp), 2008.
- [61] J. Polleux, A. Gurlo, N. Barsan, U. Weimar, M. Antonietti, and M. Niederberger, “Template-Free Synthesis and Assembly of Single-Crystalline Tungsten Oxide Nanowires and their Gas-Sensing Properties,” *Angew Chem Int Ed*, vol. 45, pp. 261-265, 2006.

- [62] A. Ponzoni, E. Comini, and G. Sberveglieri, “Unltrasensitive and High Selective Gas Sensors Using Three-Dimensional Tungsten Oxide Nanowire Networks,” *Appl Phys Lett*, vol. 88, p. 203101 (3 pp), 2006.
- [63] J.-J. Shyue, R.E. Cochran, and N.P. Padture, “Transparent-Conducting, Gas-Sensing Nanostructures (Nanotubes, Nanowires, and Thin Films) of Titanium Oxide Synthesized at Near-Ambient Conditions,” *J Mater Res*, vol. 21, pp.2894-2903, 2006.
- [64] Z. Li, M. Wu, T. Liu, C. Wu, Z. Jiao, and B. Zhao, “Preparation of TiO₂ Nanowire Gas Nanosensor by AFM Anode Oxidation,” *Ultramicroscopy*, vol. 108, pp. 1334-1337, 2008.
- [65] L.C. Tien, H.T. Wang, B.S. Kang, F. Ren, P.W. Sadik, D.P. Norton, S.J. Pearton, and J. Lin, “Room-Temperature Hydrogen-Selective Sensing Using Single Pt-Coated ZnO Nanowires as Microwatt Power Levels,” *Electrochem Solid State Lett*, vol. 8, pp. G230-G232, 2005.
- [66] S.-J. Chang, T.-J. Hsueh, I.-C. Chen, and B.-R. Huang, “Highly Sensitive ZnO Nanowire CO Sensors with the Adsorption of Au Nanoparticles,” *Nanotechnology*, vol. 19, p. 175502 (5 pp), 2008.
- [67] T.-J. Hsueh, S.-J. Chang, C.-L. Hsu, Y.-R. Lin, and I.-C. Chen, “Highly Sensitive ZnO Nanowire Ethanol Sensor with Pd Adsorption,” *Appl Phys Lett*, vol. 91, p. 053111 (3 pp), 2007.

- [68] C.S. Lao, M.-C. Park, Q. Kuang, Y. Deng, A.K. Sood, D.L. Polla, and Z.L. Wang, “Giant Enhancement in UV Response of ZnO Nanobelts by Polymer Surface-Functionalization,” *J Am Chem Soc*, vol. 129, pp. 12096-12097, 2007.
- [69] S. Song, W.-K. Hong, S.-S. Kwon, and T. Lee, “Passivation Effects on ZnO Nanowire Field Effect Transistors under Oxygen, Ambient, and Vacuum Environments,” *Appl Phys Lett*, vol. 92 p. 263109 (3 pp), 2008.
- [70] Z. Fan, D. Wang, P.-C. Chang, W.-Y. Tseng, and J.G. Lu, “ZnO Nanowire Field-Effect Transistor and Oxygen Sensing Property,” *Appl Phys Lett*, vol. 85, pp. 5923-5925, Dec. 2004.
- [71] W. Kim, and K.S. Chu, “ZnO Nanowire Field-Effect Transistor as a UV Photodetector Optimization for Maximum Sensitivity,” *Phys Status Solidi A*, vol. 206, pp. 179-182, 2009.
- [72] Y.B. Li, V.F. Della, M. Simonnet, I. Yamada, and J.J. Delaunay, “High-Performance UV Detector Made of Ultra-Long ZnO Bridging Nanowires,” *Nanotechnology*, vol. 20, p. 045501 (5 pp), 2009.
- [73] J. Zhou, Y.D. Gu, Y.F. Hu, W.J. Mai, P.H. Yeh, G. Bao, A.K. Sood, D.L. Polla, and Z.L. Wang, “Gigantic Enhancement in Response and Reset Time of ZnO UV Nanosensor by Utilizing Schottky Contact and Surface Functionalization,” *Appl Phys Lett*, vol. 94, p. 191103 (3 pp), 2009.

- [74] M.C. Jeong, B.Y. Oh, W. Lee, and J.M. Myoung, “Optoelectronic Properties of Three-Dimensional ZnO Hybrid Structure,” *Appl Phys Lett*, vol. 86, p. 103105 (3 pp), 2005.
- [75] J.B.K. Law and J.T.L. Thong, “Simple Fabrication of a ZnO Nanowire Photodetector with a Fast Photoresponse Time,” *Appl Phys Lett*, vol. 88, p. 133114 (3 pp), 2006.
- [76] Y. Li, F.D. Valle, M. Simmonnet, I. Yamada, and J.-J. Delaunay, “Competitive Surface Effects of Oxygen and Water on UV Photoresponse of ZnO Nanowires,” *Appl Phys Lett*, vol. 94, p. 023110 (3 pp), 2009.
- [77] Y.S. Yoon, H.Y. Park, Y.C. Lim, K.G. Choi, K.C. Lee, G.B. Park, C.J. Lee, D.G. Moon, J.I. Han, Y.B. Kim, and S.C. Nam, “Effects of Parylene Buffer Layer on Flexible Substrate in Organic Light Emitting Diode,” *Thin Solid Films*, vol. 513, pp. 258-263, Aug. 2006.
- [78] M.H. Huang, S. Mao, H. Feick, H. Yan, Y. Wu, H. Kind, E. Weber, R. Russo, P. Yang, “Room-Temperature Ultraviolet Nanowire Nanolasers,” *Science*, vol. 292, pp. 1897-1899, Jun. 2001.
- [79] J.H. Moon, J.H. Kim, K.-J. Kim, T.-H. Kang, B. Kim, C.-H. Kim, J.H. Hahn, and J.W. Park, “Absolute Surface Density of the Amine Group of the Aminosilylated Thin Layers: Ultraviolet-Visible Spectroscopy, Second Harmonic Generation, and Synchrotron-Radiation Photoelectron Spectroscopy Study,” *Langmuir*, vol. 13, pp. 4305-4310, 1997.

- [80] W. James, "Aptamers" in *Encyclopedia of Analytical Chemistry*, R.A. Meyers, Ed., Chichester: John Wiley and Sons Ltd., 2000, pp. 4848-4871.
- [81] T.-C. Chiu and C.-C. Huang, "Aptamer-Functionalized Nano-Biosensors," *Sensors*, vol. 9, pp. 10356-10388, 2009.
- [82] G. Arslan, M. Özmen, B. Gündüz, X. Zhang, and M. Ersöz, "Surface Modification of Glass Beads with an Aminosilane Monolayer," *Turk J Chem*, vol. 30, pp. 203-210, 2006.
- [83] Y. Han, D. Mayer, A. Offenhäusser, and S. Ingebrandt, "Surface Activation of Thin Silicon Oxides by Wet Cleaning and Silanization," *Thin Solid Films*, vol. 510, pp. 175-180, Jul. 2006.
- [84] P.-C. Chen, S. Sukcharoenchoke, K. Ryu, L.G. de Arco, A. Badmaev, C. Wang, and C. Zhou, "2,4,6-Trinitrotoluene (TNT) Chemical Sensing Based on Aligned Single-Walled Carbon Nanotubes and ZnO Nanowires," *Adv Mater*, vol. 22, pp. 1900-1904, 2010.
- [85] J. Cheng, X. Zhang, and Z. Luo, "Aligned ZnO nanorod Arrays Fabricated on Si Substrate by Solution Deposition," *Physica E Low Dimens Syst Nanostruct*, vol. 31, pp. 235-239, Mar. 2006.
- [86] L.E. Greene, B.D. Yuhas, M. Law, D. Zitoun, and P. Yang, "Solution-Grown Zinc Oxide Nanowires," *Inorg Chem*, vol. 45, pp. 7535-7543, Sep. 2006.

- [87] J. Yang, J. Yang, L. Yang, Y. Shang, D. Wang, H. Fan, H.. Liu, Y. Wang, and M. Gao, “Low-temperature Growth and Optical Properties of ZnO Nanowires,” *J Alloys Compd*, vol. 450, pp. 521-524, Feb. 2008.
- [88] A. Mason, T. Waggoner, S. Smith, J.F. Conley, Jr., and B. Gibbons, “Hydrothermal Synthesis of Zinc Oxide Nanowire on Kevlar using ALD and Sputtered ZnO Seed Layers,” in *Semiconductor Nanowires - Growth, Size-Dependent Properties, and Applications*, edited by Ali Javey (Mater. Res. Soc. Symp. Proc. Volume 1178E, Warrendale, PA, 2009) 1178-AA06-38.
- [89] S.-H. Hu, Y.-C. Chen, C.-C. Hwang, C.-H. Peng, and D.-C. Gong, “Development of a Wet Chemical Method for the Synthesis of Arrayed ZnO Nanorods,” *J Alloys Compd*, vol. 500, pp. L17-L21, Jun. 2010.
- [90] S.A. Morin, M.J. Bierman, J. Tong, and S. Jin, “Mechanism and Kinetics of Spontaneous Nanotube Growth Driven by Screw Dislocations,” *Science*, vol. 328, pp. 476-480, Apr. 2010.
- [91] Y. Qin, X. Wang, and Z.L. Wang, “Microfibre-nanowire Hybrid Structure for Energy Scavenging,” *Nature*, vol. 451, pp. 809-813, Feb. 2008.
- [92] S. Baruah and J. Dutta, “Hydrothermal Growth of ZnO Nanostructures,” *Sci Technol Adv Mater*, vol. 10, p. 013001 (18 pp.), Jan. 2009.
- [93] J. Song and S. Lim, “Effect of Seed Layer on the Growth of ZnO Nanorods,” *J Phys Chem C*, vol. 111, pp. 596-600, 2007.

- [94] M. Breedon, M.B. Rahmani, S.-H. Keshmiri, W. Wlodarski, and K. Kalantar-zadeh, "Aqueous Synthesis of Interconnected ZnO Nanowires using Spray Pyrolysis Deposited Seed Layers," *Mater Lett*, vol. 64, pp. 291-294, Feb. 2010.
- [95] J.H. Lee, I.C. Leu, and M.H. Hon, "Substrate Effect on the Growth of Well-Aligned ZnO Nanorod Arrays from Aqueous Solution," *J Cryst Growth*, vol. 275, pp. e2069-e2075, Feb. 2005.
- [96] S.-Y. Lee, T. Chen, J. Wan, G.-P. Ru, B.-Z. Li, and X.-P. Qu, "The Effect of Pre-Annealing of Sputtered ZnO Seed Layers on Growth of ZnO Nanorods through a Hydrothermal Method," *Appl Phys A: Mater Sci Process*, vol. 94, pp. 775-780, Nov. 2009.
- [97] *Powder Diffraction File* (International Center for Diffraction Data, Swarthmore, PA, 2004), JCPDS card No. 24-1467.
- [98] L. Zhang, H. Yang, J. Ma, L. Li, X. Wang, L. Zhang, S. Tian, and X. Wang, "Controllable Synthesis and Shape-dependent Photocatalytic Activity of ZnO Nanorods with a Cone and Different Aspect Ratios and of Short-and-fat ZnO Microrods by Varying the Reaction Temperature and Time," *Appl Phys A: Mater Sci Process*, vol. 100, pp. 1061-1067, May 2010.
- [99] A. Qurashi, M.F. Hossain, M. Faiz, N. Tabet, M.W. Alam, and N. Reddy, "Fabrication of Well-aligned and Dumbell-shaped Hexagonal ZnO Nanorod

Arrays and Their Dye Sensitized Solar Cell Applications,” *J Alloys Compd*, vol. 503, pp. L40-L43, Aug. 2010.

[100] M.J. Collins, Jr., “Future Trends in Microwave Synthesis,” *Future Med Chem*, vol. 2, pp. 151-155, 2010.

[101] M.-Y. Choi, D. Choi, M.-J. Jin, I. Kim, S.-H. Kim, J.-Y. Choi, S.Y. Lee, J.M. Kim, and S.-W. Kim, “Mechanically Powered Transparent Flexible Charge-Generating Nanodevices with Piezoelectric ZnO Nanorods,” *Adv Mater*, vol. 21, pp. 2185-2189, Jun. 2009.

